Schulze et al. (2018) – Supplemental Information

Table S1: Detection limits determined for major NR-PM_1 species measured during the campaign.

	Org.	SO_4	NH_4	NO_3	Chl.	MSA
Detection limit ($\mu g\ m^{-3}$)	0.12	0.019	0.005	0.009	0.011	0.002
Measurements below det. lim.	0%	0%	0%	0%	16%	1%

PMF Analysis.

The PMF model de-convolves individual component mass spectra by solving:

$$X = \sum_{k=1}^{P}\left(G_{ik} * F_{kj}\right) + E_{ij} \quad \text{(S1)}$$

where *X* is an *i x j* matrix that describes the signal of every organic mass-to-charge ratio *(j)* at each time step (*i*), *F* is a *k x j* matrix in which the rows (*k)* represent each of the factor profiles (i.e., constant mass spectra), *G* is an *i x k* matrix that describes the contribution of each factor (*k*) at each time step (*i*), and *E* is the residual matrix. The PMF model does not require any initial (*a priori*) assumptions about the factor mass spectra, but it does force each factor to be non-negative. In order to produce a single solution for a specified number of factors, the algorithm iteratively minimizes

$$Q = \sum_i \sum_j (E_{ij}/S_{ij})^2 \quad \text{(S2)}$$

where S_{ij} is the recorded HR-ToF-AMS measurement error, thereby weighting the model residuals. Data preparation including minimum counting error and variable down-weighting followed the recommendations of Ulbrich et al. (2009) and Zhang et al. (2011). Analysis of PMF results is an inherently complex process, and true factor identification often involves rigorous analysis of factor time series, diurnal trends, correlation with specific tracers, and elemental ratios (Zhang et al., 2011).

Selection of PMF factor number, fPeak value, and SEED.

According to Ulbrich et al. (2009) and the numerous examples of PMF analysis in the literature (Setyan et al., 2012; Crippa et al., 2013; Hayes et al., 2013; Schmale et al., 2013), a few specific mathematical tools are commonly used to aid with PMF factor selection. The first analyzed metric is often the sum of the squares of scaled residuals, or Q (equation (S2)). As additional factors are added to a PMF solution, the value of Q divided by Q_{exp}, or the "expected" minimum sum of squared residuals based on measurement error, should approach unity (Ulbrich et al., 2009). While a value of unity is rarely achieved in practice, a large decrease in the value of Q/Q_{exp} with the addition of another factor indicates that the additional factor explains a considerable amount of the remaining variance in the dataset, and therefore deserves inclusion within the solution. Typically, a large change in the slope of the Q/Q_{exp} versus factor number plot (Figure S1) from one number to the next (e.g., 3 to

4) is used as a qualitative metric to support this analysis (Ulbrich et al., 2009). In the dataset presented here, Q/Q_{exp} shows a considerable decrease with the addition of each factor up to the four-factor solution, after which the change is minor (Figure S1), suggesting at least four factors should be included.

The residuals produced for both individual mass-to-charge ratios as well as throughout the entire time series are also frequently used to aid solution interpretation (Ulbrich et al., 2009; Schmale et al., 2013). When moving from a two- to a three-factor solution, a considerable reduction is observed in the residual time series, as major OA spikes resulting from primary sources are incorporated into a hydrocarbon-like OA (HOA) factor (Figure S2). However, after inclusion of three factors, only individual ions (29, 40, 73, etc.) show a meaningful reduction in their residuals with additional factors. Information regarding solutions with varying numbers of factors included is provided in Table S2.

Adding a fourth factor significantly improves the overall interpretability of the PMF solution. In the 3-factor case, one factor is obviously a HOA-type component, a second (termed OOA-2 in the five-factor solution) is produced by continental sources and is highly dependent on photochemistry (substantial correlation with O_x), but the third (OOA-3 in the five-factor solution) shows no significant correlation with any tracers (Table S3). In addition, apportioning the third factor to either a specific source location or a regional production mechanism is difficult, as it represents the majority of OA during the marine period, when there is little diurnal variation in total OA, as well as during the frontal/LP period, when significant diurnal variation exists. However, adding a fourth factor considerably improves the correlation between OOA-3 and SO_4 (as well as NH_4) (ΔR^2 = 0.25-0.3), and causes OOA-3 to represent a majority of OA during only the marine period, leading to more definitive characterization of OOA-3 as an OA factor produced over the Gulf of Mexico. As a result, the solution contains a primary factor (HOA), a continental factor (OOA-2), a marine factor (OOA-3), and a fourth factor (OOA-1) that accounts for the majority of OA mass directly following a storm event when only aged regional highly processed OA should be present. While OOA-1, OOA-2, and OOA-3 have highly correlated mass spectra due to their highly aged nature (large signal at m/z 28 and 44), the correlations are significantly reduced if these signals are removed (R^2 ~0.5-0.7), while their time series are distinct ($R^2 < 0.31$) and show no indications of simple factor splitting.

Moving to a five factor solution produces a component that is highly correlated with nitrate (R^2 = 0.85), has a moderate O:C ratio (0.41), and correlates well with previously extracted SV-OOA components (Docherty et al., 2011; Setyan et al., 2012) (Table S4), justifying its inclusion within the overall solution. The previously extracted factors are only marginally affected with the inclusion of SV-OOA (Table S3). However, a six-factor solution results in two factors with nearly identical time series (R^2 = 0.88) and similar mass spectra (R^2 = 0.65), and further analysis indicates that the original OOA-2 factor has been split (Figure S3). Additionally, the mass spectra of the original OOA-1 factor (4^{th}) shows prominent signal at only two m/z (29 and 40) and has a time series and diurnal profile that cannot be easily interpreted.

After varying the fPeak parameter, a final value of 0, with a minimum Q/Q_{exp} was chosen. Positive values of the fPeak parameter (0.5-3.0) transform OOA-1 into a factor composed primarily of m/z 29 and 40, with m/z 29 comprising 30% of the overall mass spectra, resulting in a physically unrealistic and uninterpretable factor. In appearance, this factor is similar to the third factor produced in the six-factor solution (Figure S3). A similar transformation was observed by Schmale et al. (2013) for positive fPeak values when interpreting coastal measurements on Bird Island near Antarctica. Negative values of fPeak, which tend to increase the correlation between factor mass spectra while decreasing correlation between factor time series, produce rapid variation in OOA-1 and OOA-3 during the marine period, causing a reduction in the correlation between OOA-3 and SO_4 from 0.55 (fPeak = 0) to 0.28 (fPeak = -3.0) (Figure S4) with no corresponding increases in the interpretability of any of the remaining factors.

SEED values, representing pseudo-random starting points for the PMF algorithm, from 0-30 were examined (with a SEED-step value of 2). In general, the solutions were very stable, with little change in either the mass fraction of different factors or the correlations with external tracers as SEED values changed. However, two SEED values (4 and 28) resulted in solutions similar to those produced using positive fPeak values. While these solutions had the lowest values of Q/Q_{exp}, the alteration of the factors made OOA-1 uninterpretable and caused factor splitting of OOA-2. As a result, SEED 0 was chosen for the final solution.

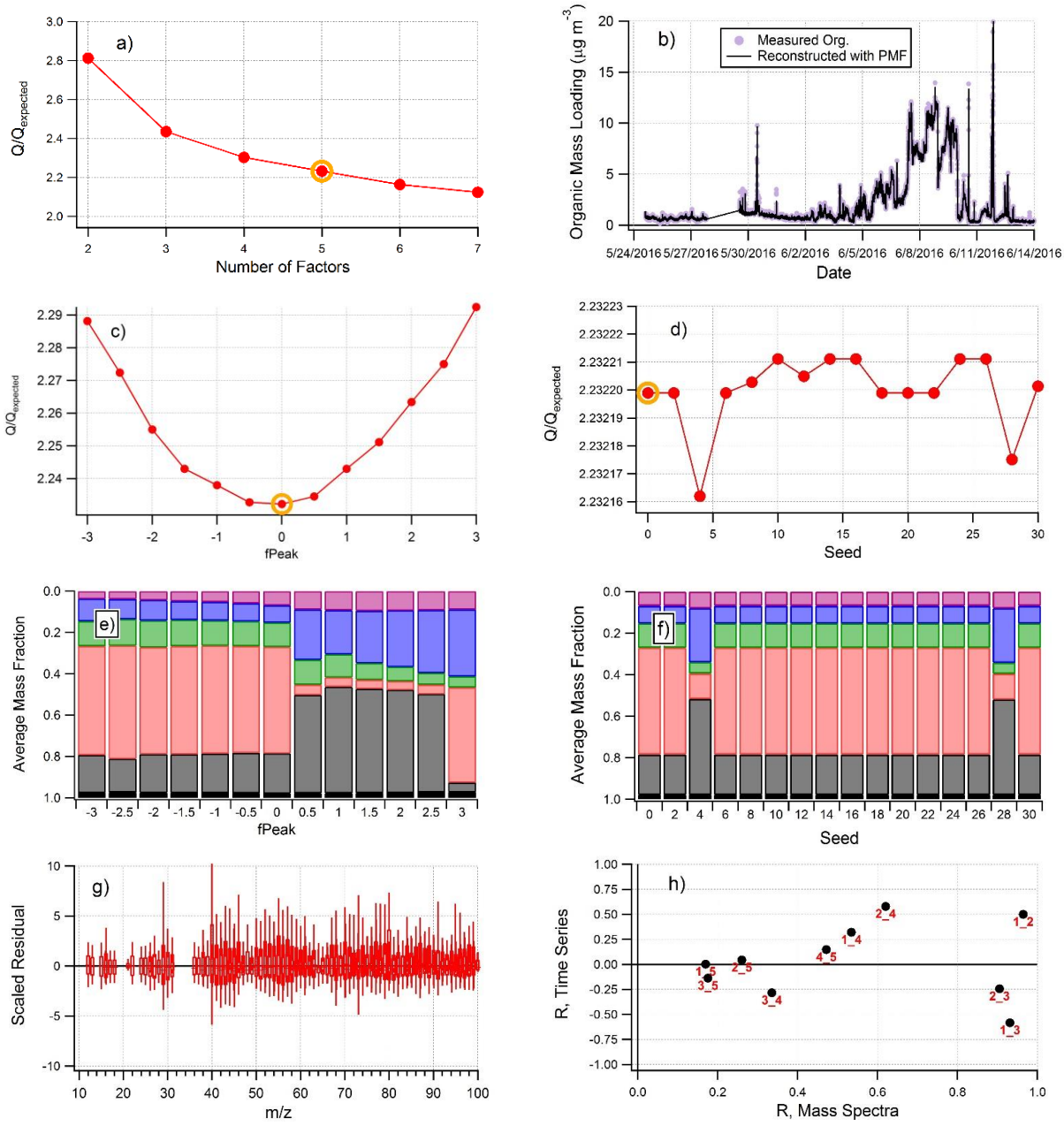

Figure S1. Evaluation of primary PMF diagnostics: (a) Q/Q_{exp} as a function of the number of factors tested within the dataset. The final chosen 5-factor solution is highlighted. (b) Measured time series of OA mass loading, along with reconstructed time series using sum of PMF solutions. (c) Variation in Q/Q_{exp} as a function of fPeak parameter. (d) Variation in Q/Q_{exp} as a function of SEED value. (e) Average mass fraction of each factor as a function of fPeak parameter (the large change in OOA-1 and OOA-2 with positive fPeak is due to the fact that these two factors essentially switch (i.e. OOA-1 becomes OOA-2 and vice versa at fPeak 0.5-2.5). (f) Average mass fraction of each factor as a function of SEED value. (g) Overall scaled residual at each m/z. (h) Correlation of factor time series and mass spectra with other extracted factors.

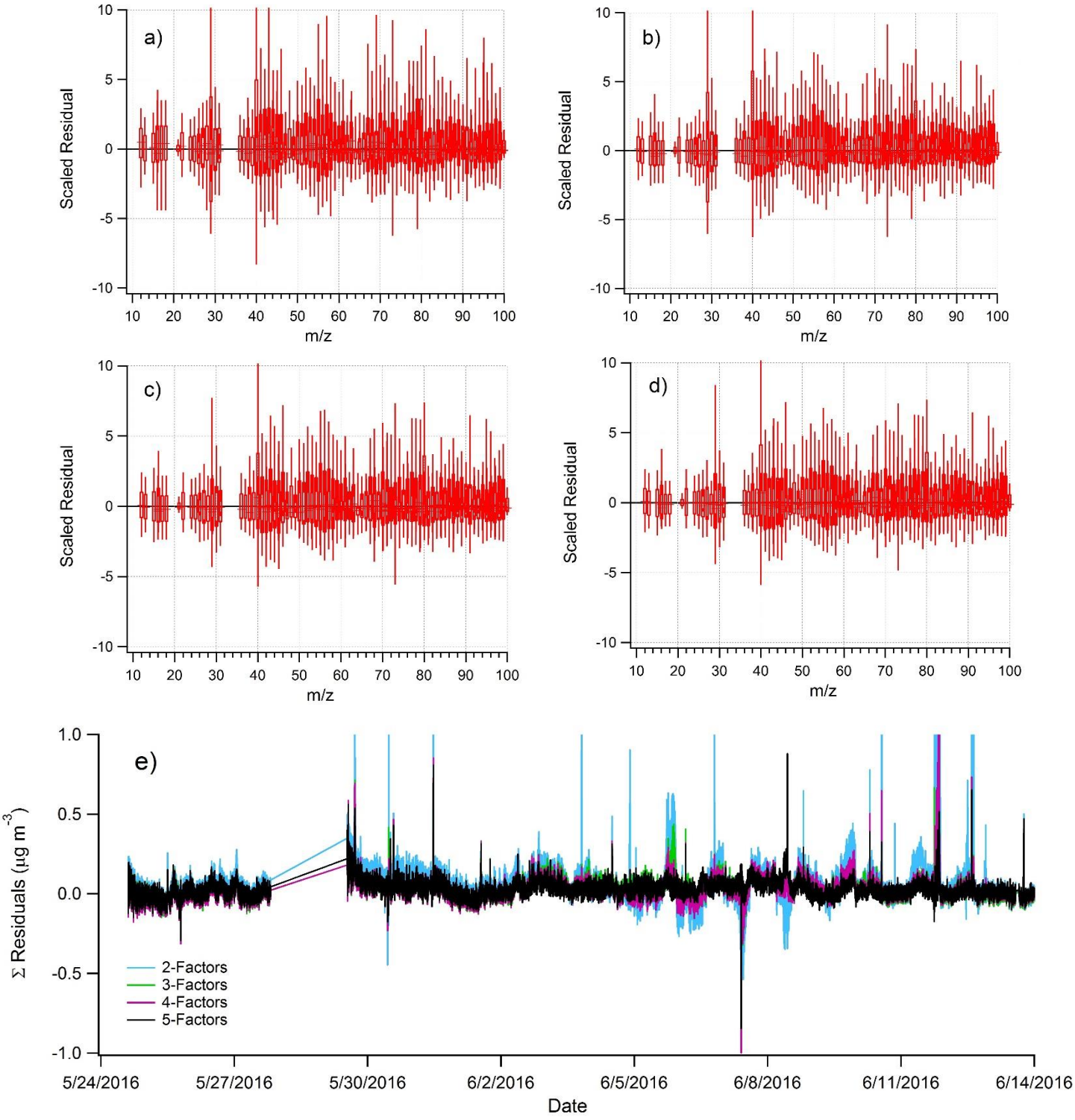

Figure S2: (Top) Scaled residuals of each m/z (10-100) for the 2-factor (a) through 5-factor (d) solution. (Bottom) Time series of the sum of residuals for 2-5 factors.

Table S2: Abbreviated description of PMF factor selection process

Factor	fPeak	Q/Q_{exp}	Factors resolved*	Reason for selection/rejection
2	0	2.812	OOA-2, OOA-3	Large change in slope of Q/Q_{exp} vs. factor number from 2-3 factors suggests need for third factor.
3	0	2.389	OOA-2, OOA-3, HOA	Another large change in slope of Q/Q_{exp} vs. factor number from 3-4 factors suggests need for fourth factor. Some noticeable residual removed during frontal/LP period in the middle of the campaign. Improved interpretability of OOA-3 when moving to 4-factor solution (much larger correlation with SO_4 and NH_4).
4	0	2.303	OOA-1, OOA-2, OOA-3, HOA	Despite only a subtle lack of major change in slope of Q/Q_{exp} when moving from 4- to 5-factor solution, an obvious SV-OOA factor is revealed in 5-factor solution.
5	0	2.232	OOA-1, OOA-2, OOA-3, HOA, SV-OOA	Optimal possible solution. Each factor can reasonably be attributed to a specific source (e.g., OOA-3 to mixture of shipping and biogenic marine emissions), and moving to a 6-factor solution results in factor splitting.
6	0	2.163	-	Extraction of 6-factor solution results in factor splitting, whereby new factor correlates almost perfectly with time series of OOA-2 and mass spectra of SV-OOA. In addition, OOA-1 factor becomes less interpretable.

*The names of "Factors resolved" correspond to factors in the final solution that most closely resemble factors extracted in the given solution. For instance, OOA-2 in the 2-factor solution is named for its similarity to OOA-2 in the final 5-factor solution.

Table S3: Correlation of resolved factors (R^2) with non-refractory aerosol species, trace gases, and meteorological variables.

Factor	Solution	Org	SO_4	NH_4	NO_3	Chl	O_3	NO_x	CO	Temp	RH	WS
	3-factor	-	-	-	-	-	-	-	-	-	-	-
OOA-1	4-factor	0.40	0.02	0.02	0.36	0.03	0.49	0.07	0.05	0.07	0.00	0.00
	5-factor	0.32	0.01	0.01	0.15	0.04	0.43	0.02	0.01	0.04	0.01	0.00
	3-factor	0.95	0.00	0.01	0.42	0.00	0.50	0.03	0.01	0.00	0.05	0.10
OOA-2	4-factor	0.94	0.01	0.02	0.39	0.00	0.57	0.02	0.01	0.00	0.05	0.11
	5-factor	0.93	0.01	0.02	0.33	0.00	0.46	0.01	0.01	0.00	0.06	0.12
	3-factor	0.13	0.38	0.33	0.08	0.01	0.10	0.04	0.00	0.00	0.00	0.01
OOA-3	4-factor	0.04	0.62	0.60	0.08	0.06	0.18	0.07	0.00	0.07	0.02	0.01
	5-factor	0.08	0.55	0.55	0.05	0.08	0.24	0.04	0.00	0.06	0.00	0.01
	3-factor	-	-	-	-	-	-	-	-	-	-	-
SV-OOA	4-factor	-	-	-	-	-	-	-	-	-	-	-
	5-factor	0.44	0.00	0.00	0.85	0.00	0.27	0.19	0.01	0.03	0.00	0.01
	3-factor	0.13	0.01	0.00	0.07	0.00	0.10	0.15	0.01	0.00	0.00	0.00
HOA	4-factor	0.11	0.01	0.01	0.06	0.00	0.08	0.15	0.00	0.00	0.00	0.00
	5-factor	0.07	0.01	0.01	0.02	0.00	0.03	0.10	0.00	0.00	0.00	0.00

Table S4: Correlation of PMF factor mass spectra with previously published spectra from the HR mass spectral database (http://cires1.colorado.edu/jimenez-group/HRAMSsd/)

Reference Spectra	R^2				
	OOA-1	OOA-2	OOA-3	SV-OOA	HOA
HOA - Docherty et al. (2011)	0.07	0.14	0.04	0.48	0.82
HOA – Aiken et al. (2009)	0.01	0.04	0.01	0.28	0.74
SV-OOA – Docherty et al. (2011)	0.37	0.51	0.26	0.78	0.67
SV-OOA – Mohr et al. (2012)	0.61	0.71	0.52	0.57	0.51
LO-OOA – Setyan et al. (2012)	0.83	0.94	0.80	0.38	0.25
MO-OOA – Setyan et al. (2012)	0.73	0.84	0.56	0.70	0.25
LV-OOA – Docherty et al. (2011)	0.93	0.97	0.93	0.22	0.07
LV-OOA – Aiken et al. (2009)	0.92	0.91	0.84	0.27	0.07
OOA-a – Saarikoski et al. (2012)	0.91	0.97	0.89	0.27	0.08
OOA-b – Saarikoski et al. (2012)	0.92	0.98	0.85	0.39	0.11
OOA-c – Saarikoski et al. (2012)	0.90	0.97	0.91	0.26	0.08
MOA – Crippa et al. (2013)	0.60	0.62	0.37	0.75	0.31

SV = semi-volatile; LV = low volatility; LO = less-oxidized; MO = more-oxidized; MOA = marine organic aerosol

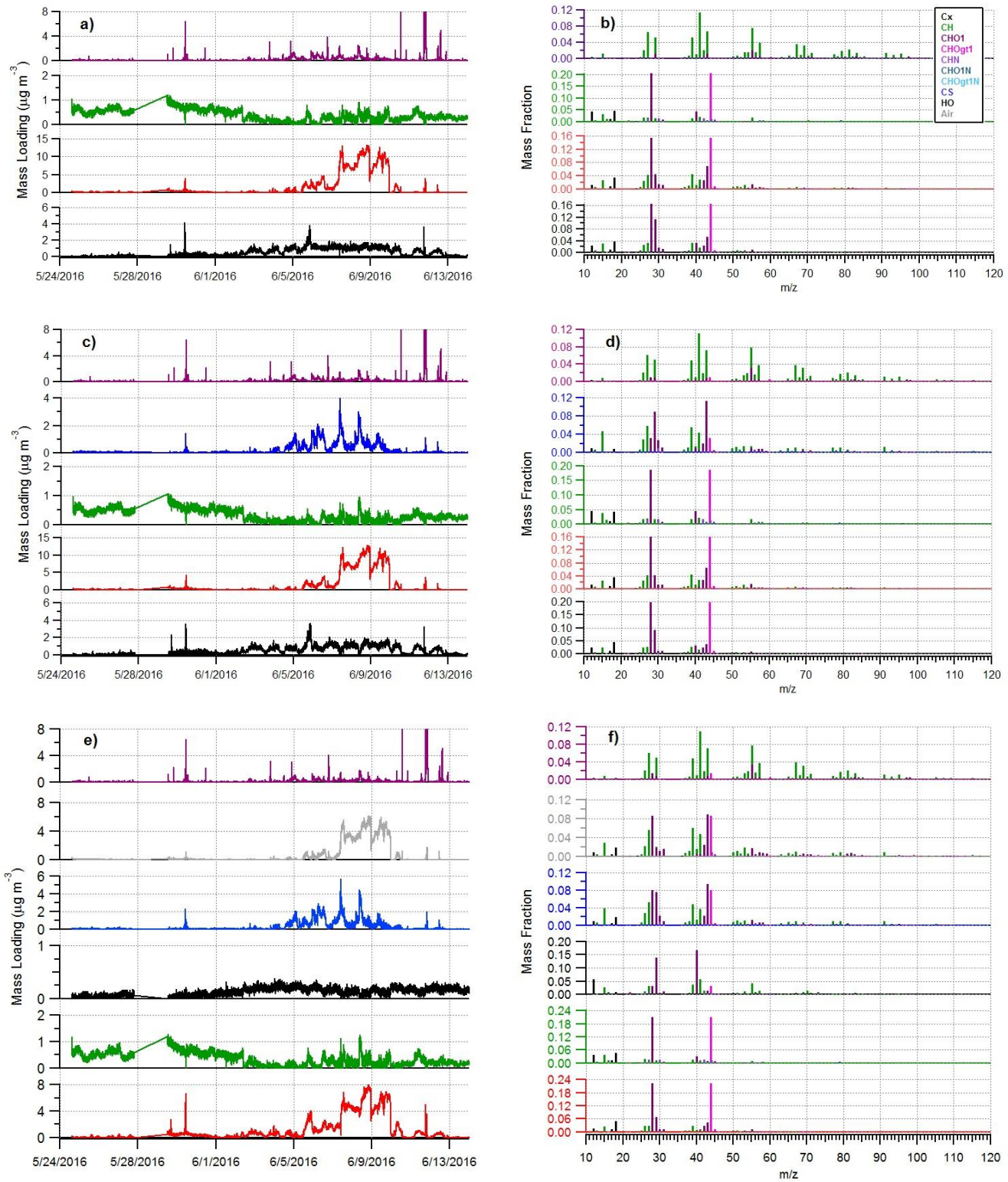

Figure S3: Comparison of time series and MS results for the 4- (a,b), 5- (c,d), and 6- (e,f) factor solutions.

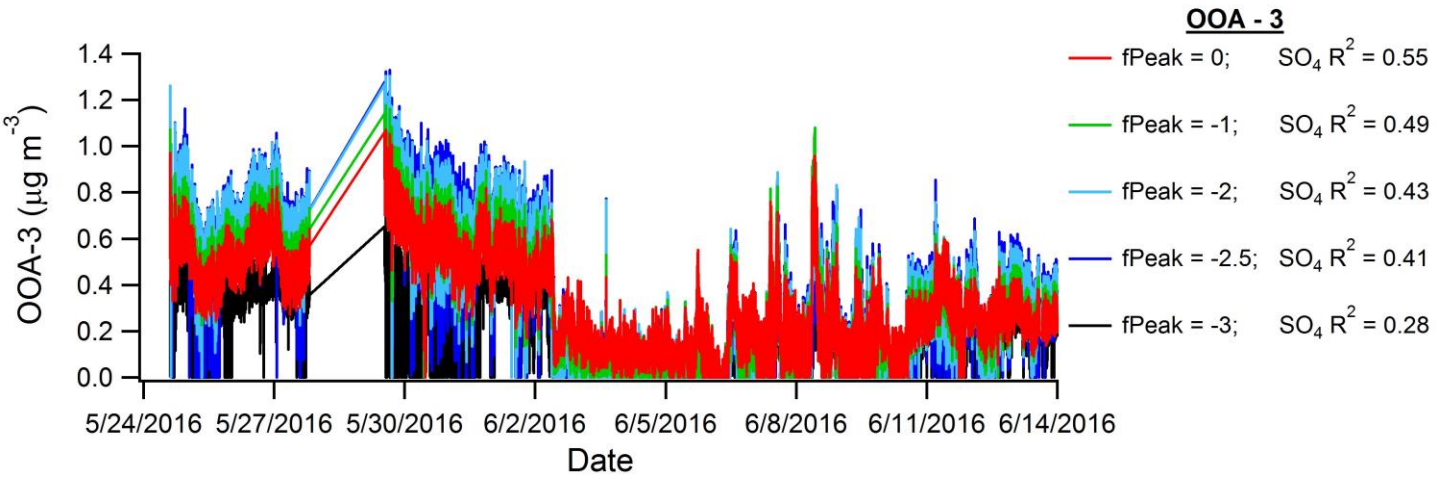

Figure S4: Time series of the OOA-3 factor for different negative values of the fPeak parameter. The corresponding correlation with SO_4 is also shown.

Source Apportionment of Organic Aerosol – PMF Factor Descriptions

Applying PMF and varying the potential number factors from 2 to 7 revealed an optimal five-factor solution, as discussed above. The five factors extracted by the PMF model correspond to HOA, a SV-OOA, and three more oxygenated organic aerosols (OOA-1, OOA-2, and OOA-3). The mass spectra and time series of each factor are provided in Figures S5 and S6. A brief description of each factor is included below.

Hydrocarbon-like OA (HOA).

A HOA factor has been identified in urban campaigns in the literature (Ng et al., 2010) and during previous studies in Houston specifically (Bates et al., 2008; Cleveland et al., 2012; Wallace et al., 2018). The HOA factor correlates well ($R^2 > 0.7$) with the ion series $C_nH_{2n-1}^+$ and $C_nH_{2n+1}^+$, which are typical fragments of branched alkanes and cycloalkanes and are a common characteristic of OA mass spectra from primary emission sources (Canagaratna et al., 2004; Mohr et al., 2009). The HOA mass spectrum presented also correlates well with previously published HOA spectra from Riverside, California ($R^2 = 0.82$) and Mexico City ($R^2 = 0.74$) (Aiken et al., 2009; Docherty et al., 2011), supporting its attribution to primary sources.

The O:C value of HOA (0.07) is very low, suggesting it is composed primarily of reduced hydrocarbons; however, it is between the values reported for directly measured diesel vehicular emissions (0.03-0.04) and those for meat-cooking OA (COA, 0.11-0.14) (Mohr et al., 2009), implying that the measured HOA is either slightly oxygenated vehicular emissions, a combination of vehicular emissions and COA, or both. While the time series of HOA and NO_x are visually very similar, multiple spikes in HOA mass during the marine period that are not accompanied by NO_x (but are coincident with increases in the $C_3H_3O^+$ ion, a tracer for COA) cause the overall campaign correlation between HOA and NO_x to be low ($R^2 = 0.15$) (Figure S7) (Mohr et al., 2012); however, if these periods are removed, the correlation is in line with literature values (R^2 ~0.6). As measurements were performed at a location surrounded by private homes, local cooking may have impacted the measurements.

As expected, HOA contributes most noticeably to OA (on a mass basis) during the continental period, with an average mass loading (0.16 μg m^{-3}, 2.6% of OA) smaller than that measured by Cleveland et al. (2012) near

downtown (1.7 μg m^{-3}; 32%) and by Wallace et al. (2018) (0.67 μg m^{-3}; 16%) within the HSC, due to the lack of large highways near the site. The small amount of HOA measured during marine periods also confirms that the site is not heavily influenced by fresh shipping emissions, as multiple studies have reported an HOA-like signature when directly measuring ship exhaust (Murphy et al., 2009; Diesch et al., 2013).

Semi-volatile Oxygenated OA (SV-OOA)

The SV-OOA factor is characterized by a moderate O:C ratio (0.41), a smaller f_{44}:f_{43} ratio than the more oxygenated factors (Ng et al., 2010), and significant correlation with nitrate aerosol (R^2 = 0.85), all of which align with previous SV-OOA components in the literature (Crippa et al., 2013; Hayes et al., 2013; Xu et al., 2014; Xu et al., 2016). In addition, the mass spectrum of SV-OOA correlates well with previously published SV-OOA factors (Table S4). It is important to note that the distinction as "semi-volatile" is based on similarity with the literature rather than actual volatility measurements, which were not available during the campaign. Similarly to HOA, SV-OOA mass loadings are only significant (on a mass basis) during the continental period, implying either a lack of substantial coastal (i.e., marine) SV-OOA sources or extensive aging of marine SV-OOA prior to measurement.

The sources of previously extracted SV-OOA factors are highly variable, with production linked to anthropogenic VOCs (Ng et al., 2011; Hersey et al., 2011; Hayes et al., 2013), biogenic VOCs (Setyan et al., 2012; Coggon et al., 2014; Bean et al., 2016; Leong et al., 2017), or a combination of the two, depending on measurement location. Leong et al. (2017) recently classified Houston into two distinct pollution zones based on NR-PM_1 characteristics measured in a variety of locations spanning the Houston region. Analysis of backward trajectories encountered during the continental period indicates that the majority of air masses passed through the industrial "Zone 2," suggesting that OA was influenced heavily by anthropogenic sources.

The diurnal trend of SV-OOA during the continental period supports the hypothesis of a primarily anthropogenic source. Overall during the continental period, increases in SV-OOA mass loadings in the early morning were coincident with increases in HOA mass, suggesting SV-OOA may form from the oxidation of hydrocarbons emitted from vehicles. However, the peak in mass loadings between 8:00 and 10:00, when intense

mixing between the residual layer (RL) and the nocturnal boundary layer (NBL) has been observed in Houston (Haman et al., 2014), suggests that a significant component of SV-OOA is likely the result of nocturnal transport and aging within the RL followed by subsequent down-welling during breakup of the NBL. In Lanzhou, China, a majority of the extracted SV-OOA factor was produced through such boundary layer dynamics, and the diurnal profile was nearly identical to the SV-OOA factor in this study (Xu et al., 2014). The diurnal trend of SV-OOA also suggests that its formation is not due to nighttime nitrate radical-related processing of local BVOC emissions, which has been observed in the forested areas north of Houston (Bean et al., 2016; Leong et al., 2017), as the profile displays minimum mass loadings when nitrate radical concentrations would be maximized (i.e., late evening/at night).

Previous studies have revealed that the f_{44}:f_{43} triangle plot established by Ng et al. (2010) can be used to identify anthropogenic versus biogenic influences on SV-OOA components. Specifically, SV-OOA factors associated with anthropogenic emissions typically lie to the left side of the plot, with a relatively high f_{44}:f_{43} ratio (Hersey et al., 2011; Setyan et al., 2012; Craven et al., 2013; Hayes et al., 2013), while biogenic components lie further right, with a larger fraction of non-acid oxygenated compounds (Setyan et al., 2012; Han et al., 2014; Coggon et al., 2014). Figure S8 displays these regions, along with an area representing factors likely impacted by a mixture of sources. When extracted from the entire dataset, SV-OOA lies in the mixed region, with a relatively low ratio of f_{44}:f_{43}, similar to the average SV-OOA results obtained from six sites by Ng et al. (2011). However, when PMF is applied to only the continental period, the extracted SV-OOA factor much more closely resembles previously reported factors related to oxidation of urban traffic emissions (Figure S8) (Hersey et al., 2011; Setyan et al., 2012; Craven et al., 2013; Hayes et al., 2013). As a result, similarly to HOA, when SV-OOA mass loadings are notable in this environment (i.e. > 0.5 μg m^{-3}) urban emissions appear to be responsible for its production.

Oxygenated OA – 1 (Highly Oxidized OA)

The three OOA factors were ranked (1 to 3) based on their O:C ratios. While the O:C ratio of OOA-1 (1.15) is at the upper end of PMF components found in the literature (Ng et al. 2010; Hayes et al., 2013), its time series

does not correlate particularly well with either SO_4 (R^2 = 0.03) or O_x (O_3 + NO_2) (R^2 = 0.54), as is typical of highly aged components (Hayes et al., 2013). Typically, large O:C ratios signify factors that have undergone extensive atmospheric processing during multiple days of transport to the measurement site (Chen et al., 2015; Ortega et al., 2016) or regionally distributed, relatively invariant background components (Hayes et al., 2013). The OOA-1 factor dominated total OA mass during the frontal/LP period, after a rainstorm had scavenged the majority of ambient NR-PM_1. The O:C value (1.15) and f_{44} (0.19) of OOA-1 are similar to the highly aged background marine aerosol factor extracted by Schmale et al. (2013) near Antarctica (O:C = 1.05; f_{44} = 0.22).

While the aged nature of OOA-1 prevents its mass spectra from revealing major information about its sources, a few specific characteristics suggest a possible role for WSOG. Perhaps most notably, OOA-1 contains the largest fractional contribution from m/z 29 (CHO^+) (0.1) of all of the OOA factors, which is an aldehyde tracer (Faust et al., 2017) and atypical of highly aged components (Ng et al., 2010), as aldehyde functional groups are typically converted into carboxylic acids with atmospheric processing (Ng et al., 2011). Biomass burning OA (BBOA) is known to produce significant signal at m/z 29 (Aiken et al., 2009; Saarikoski et al., 2012); however, the lack of any appreciable signal at m/z 60 ($C_2H_4O_2^+$) or 73 ($C_3H_5O_2^+$), common fragments of levoglucosan (i.e., BBOA tracer ions) (Lanz et al., 2007; Mohr et al., 2009), suggests that biomass burning is not a major OOA-1 source. It should be noted that the standard HR-ToF-AMS data analysis correction was performed to ensure that the CHO^+ ion signal was not simply an artifact of gaseous ^{15}NN.

Both chamber and field experiments have shown that incorporation of glyoxal and methylglyoxal into deliquesced ambient aerosol significantly increases the mass fraction of the CHO^+ ion (Chhabra et al., 2010; Lee et al., 2011; Faust et al. 2017); however, these compounds produce little signal at m/z 44 unless oxidized, indicating that if glyoxal/methylglyoxal contribute to OOA-1, they are either partially oxidized or mixed with other oxidized components. In Beijing, Sun et al. (2016) extracted an aqueous OOA factor linked to glyoxal/methylglyoxal related processing that had a m/z 29 signal (0.08) and an f_{29}:f_{44} ratio (~0.7) similar to OOA-1 and much larger than the other, photochemically-produced OOA factor extracted in that study (f_{29}:f_{44} ~0.25).

Further evidence of a possible influence from WSOG is provided by the f_{29}-f_{43}-f_{44} ternary diagram (Lee et al., 2011). Lee et al. (2011) noted that in addition to the commonly utilized f_{44}:f_{43} triangle plot, the ternary diagram including f_{29} more accurately portrayed the influences of different precursor compounds (e.g., typical monoterpene SOA versus monoterpene-glyoxal mixture) on OA oxidation pathways. Figure S9 displays this f_{29}-f_{43}-f_{44} ternary diagram describing general SOA oxidation, with the extracted PMF factors and published data from anthropogenic and biogenic SOA components shown. Interestingly, the location of OOA-1 is very similar to an oxidized 2:1 glyoxal:α-pinene mixture as well as to the highly aged background marine aerosol factor extracted by Schmale et al. (2013) near Antarctica (O:C = 1.05). However, of the major classes of SOA depicted, only benzene SOA is located in a similar location in f_{29}-f_{43}-f_{44} space. As benzene concentrations over the MBL within the ECA are likely very small (Murphy et al., 2009; Lack et al., 2011), and benzene SOA typically has lower maximum O:C ratios than OOA-1 (0.6-0.8) (Sato et al., 2012), this observation further supports a possible contribution from glyoxal/methylglyoxal related processing. Furthermore, Jia and Xu (2014) observed that the dominant compounds in SOA produced from benzene photooxidation were glyoxal hydrates and carboxylic acids, supporting the location of benzene SOA on the ternary diagram. Ultimately, OOA-1 is characterized as a highly processed background species potentially influenced by WSOGs. This WSOG signature may be a result of substantial cloud processing during transport of OOA-1.

Oxygenated OA – 2 (Continental OA)

While the mass spectrum and O:C ratio of OOA-2 are both very similar to those of OOA-3, the time series are entirely distinct, with OOA-2 contributing the majority of OA mass during the continental period (Figure S6), suggesting OOA-2 production relies on continental VOC precursors. Notably, OOA-2 was highly correlated ($R^2 > 0.7$) with the oxygenated ion series $C_xH_yO_2^+$ and $C_xH_yO_1^+$, unlike the other OOA factors. In terms of gas-phase species, OOA-2 showed strong correlation with O_x, especially during the continental period ($R^2 = 0.74$), implying OOA-2 formation is linked to photochemical processing. The diurnal cycle of OOA-2 during the continental period further supports an influence of photochemistry, as it shows a distinct increase from ~8:00 to ~11:00 local time followed by a considerable decrease in the afternoon. Formation of OOA-2 may be associated with further oxidation of semi-volatile VOCs that comprise SV-OOA at night but evaporate

with increasing morning temperatures and expansion of the PBL, as OOA-2 mass loadings are steady from 11:00-13:00 local time despite a likely growing boundary layer (Haman et al., 2014), while SV-OOA mass loadings decrease considerably. During summertime measurements in downtown Houston, Cleveland et al. (2012) extracted an OOA factor that showed a similar photochemical dependence but was significantly less oxidized (O:C = 0.46 versus 0.79 in this study). As the measurements in Cleveland et al. (2012) were much closer to both vehicular and industrial VOC-emitting sources in and around the HSC, such a difference is expected, as transport away from emission sources and both daytime (photooxidation) and nighttime (nitrate radical-driven) processing should increase the O:C ratio.

The observation of a daily rapid increase after ~8:00 local time during the continental period, combined with the lack of local strong VOC sources near the measurement site (i.e., within 10 miles in any direction), suggests that OOA-2 formation, similarly to SV-OOA, may be dependent on overnight transport of industrial plumes and subsequent down-welling of precursor sources (in both the gas- and aerosol-phase) during the breakup of the NBL. Zaveri et al. (2010) previously noted that such a process was capable of causing air quality reductions (e.g., high O_3 events) in regions as far as 300 km from Houston. Specifically, the authors noted that relatively rapid horizontal wind speeds and suppressed vertical mixing in the nocturnal RL, combined with nighttime oxidation of emitted VOCs (as a result of nitrate radical production), result in fast transport of the Houston urban plume and formation of a chemical mixture capable of rapid oxidant formation (high concentrations of nitrous acid, NO_2, etc.) and SOA formation (high concentrations of semi-volatile VOCs) with sunrise and the breakup of the NBL the following morning. Observed wind directions suggest that nighttime transport of OOA-2 precursors over the ocean, down-welling over the MBL in the morning, and aging in the afternoon during transport back to the measurement site appears to play a role in OOA-2 formation, as maximum mass loadings are consistently observed during onshore flow periods (Figure S10).

Oxygenated OA – 3 (Marine OA)

OOA – 3 represents the dominant source of OA during marine periods, accounting for 55% on average, and shows little diurnal variation, implying regional rather than local production. Based on the lack of correlation

between OOA-3 and trajectory-averaged wind speed (R^2 = 0.1) and the discussion of marine OA sources in the main text, we can rule out marine POA as the major source (Russell et al., 2010).

While the least oxygenated of the three OOA factors, with an O:C of 0.77, the O:C value of OOA-3 is within the range of previously extracted marine organic aerosol factors identified in Paris by Crippa et al. (2013) (0.57), and by Schmale et al. (2013) on Bird Island (1.05) but is larger than typical bulk marine OA measured in remote locations (O:C ~0.6) (Frossard et al., 2014). The contribution of nitrogen fragments (12%) is much larger than observed during a primary marine organic plume by Ovadnevaite et al. (2011) (<1%), implying a significant influence from secondary production of amines, partially due to elevated partitioning potential as a result of increased amounts of acidic sulfate aerosol over the MBL from shipping emissions. The sulfur to carbon (S:C) ratio (0.007), is only about half as large as the S:C ratio of the marine OA factor identified by Crippa et al. (2013) but is more than an order of magnitude larger than the other factors. OOA-3 mass loadings are correlated with MSA (R^2 = 0.41), but the correlation is not nearly as strong as observed for the predominantly biogenic marine OA factor (R^2 = 0.84) extracted by Crippa et al. (2013), despite the fact that OOA-3 contains 89% of total measured MSA.

The lack of significant correlation between OOA-3 and MSA, large contribution of anthropogenic sources to nss-SO_4, and previous recognition of an influence of combustion sources on marine OA in the Gulf of Mexico suggest anthropogenic emissions contribute to OOA-3 production. The relatively weak correlations between the mass spectra of OOA-3 and those of marine biogenic OA factors extracted by Chang et al. (2011) over the Arctic Ocean (R^2 = 0.44), Crippa et al. (2013) in Paris (R^2 = 0.37), and the marine-biogenic period identified in this study (R^2 = 0.56) support this hypothesis. The mass spectra of OOA-3 is notable in its lack of significant signal at either m/z 29 or 43, implying major conversion of OA into carboxylic acid functional groups, causing OOA-3 to lie near the bottom vertex (i.e., most processed location) of the f_{29}-f_{43}-f_{44} ternary diagram (Figure S9). Notably, OOA-3 lies very near the value for naphthalene SOA (Chhabra et al., 2010) in the ternary diagram, which multiple studies have confirmed is a major VOC emitted by container ships burning heavy fuel oil (Murphy et al., 2009; Czech et al., 2017). The O:C and H:C ratio of OOA-3 (0.77 and 1.42, respectively) also align well with the corresponding ratios of photo-oxidized aromatic species such as toluene

and m-xylene (O:C = 0.66-0.74; H:C = 1.38-1.54) (Chhabra et al., 2010), which are also emitted in large quantities by container shipping vessels (Murphy et al., 2009).

The WPSCF plot of OOA-3 provides further evidence of an influence from shipping vessels (Figure S11), as a region of high probability exists over the area of shipping lane convergence, as seen for anthropogenic nss-SO_4. The spearman rank-order correlation coefficient (r_s) between the OOA-3 WPSCF grid and the anthropogenic nss-SO_4 grid ($r_s = 0.96$) is greater than that between OOA-3 and MSA ($r_s = 0.82$).

These results are supported by Figure S12, which shows strong correlation between anthropogenic SO_4 and OOA-3 during marine periods ($R^2 > 0.75$) when grouped by overall trajectory length (in order to account for potential spurious correlation due to processing time during transport). The correlation between OOA-3 and anthropogenic nss-SO_4 implies that OOA-3 formation is associated either directly with anthropogenic sources through oxidation of shipping emissions, as suggested by the mass spectral indicators discussed above, or indirectly through enhanced secondary formation of marine biogenic OA due to increased oxidant levels, ALW, or OA (i.e., increased partitioning potential of SVOCs). Some evidence of the indirect process is provided by the noticeable contribution from MSA and the high mass fraction of nitrogen-containing fragments. Assuming, as a strictly upper-bound estimate, that OOA-3 production is entirely driven by shipping emissions, the combination of anthropogenic nss-SO_4, NH_4, and OOA-3 implies that a maximum of 71% of total marine NR-PM_1 measured over the Gulf of Mexico was the result of anthropogenic sources during this study, supporting the need for further regulations on global shipping fuel sulfur content.

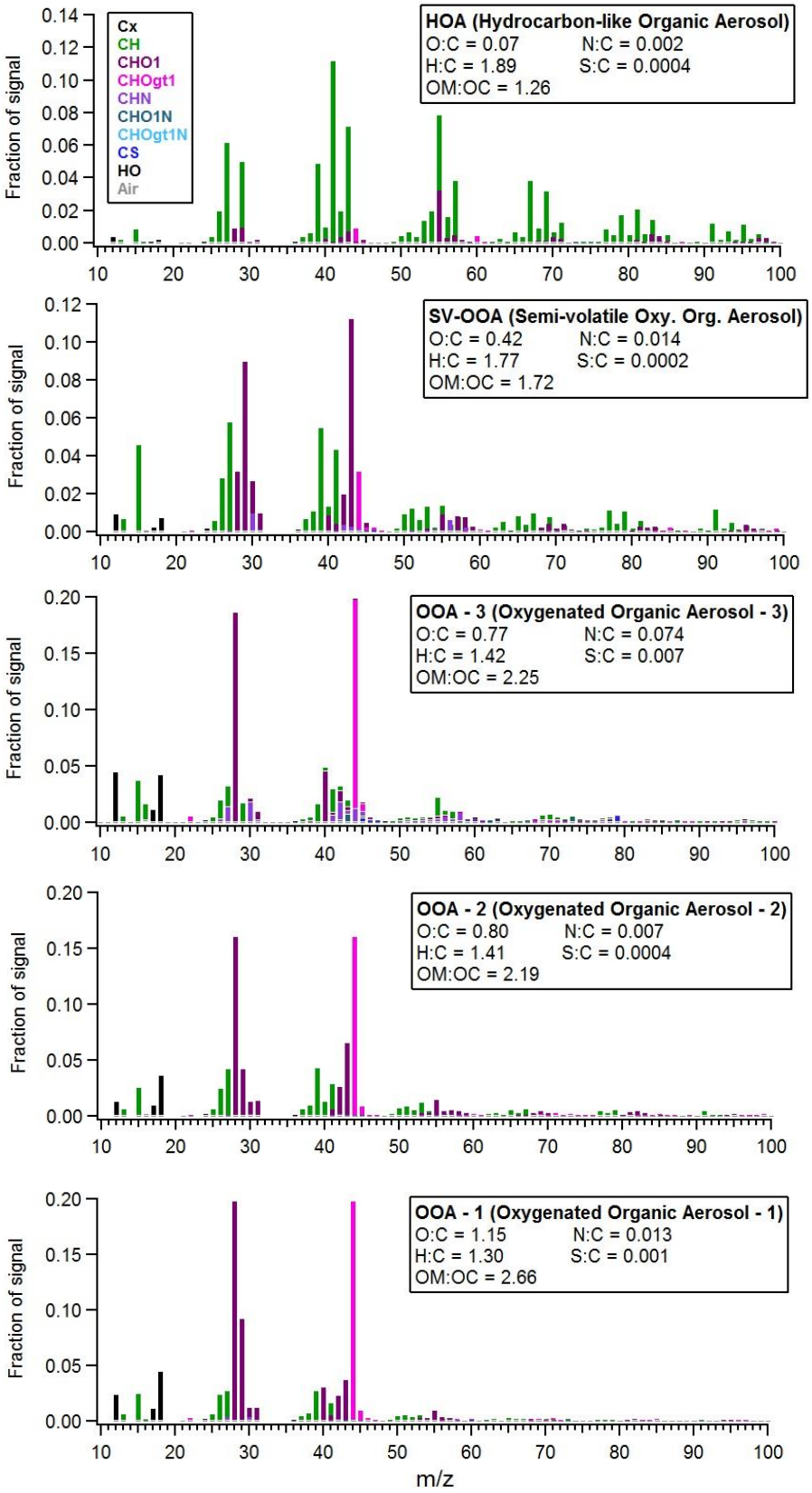

Figure S5: High resolution mass spectra of five OA factors extracted with PMF analysis.

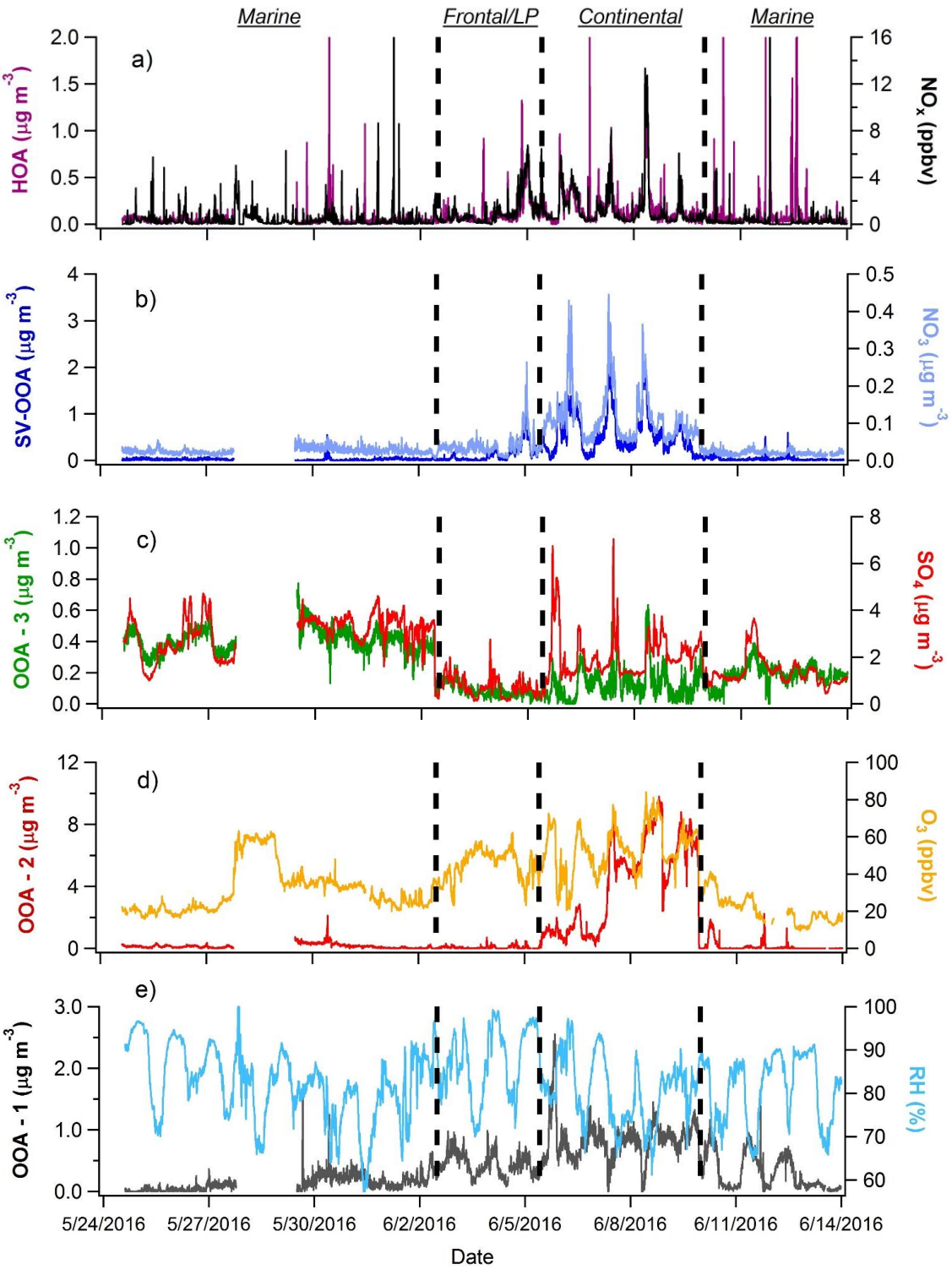

Figure S6: Time series of identified PMF factors and additional ancillary data used for factor identification.

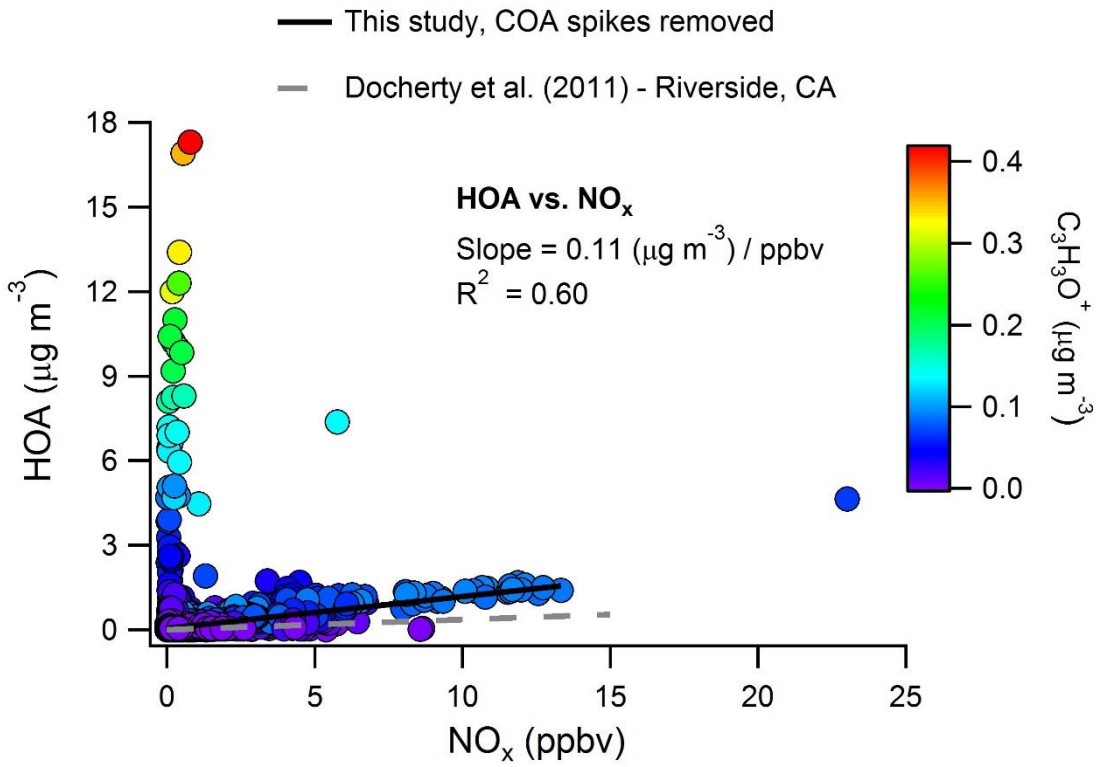

Figure S7: Correlation between HOA and NO_x. Rapid increases in HOA due to localized cooking (using $C_3H_3O^+$ as a tracer ion) cause poor overall correlation between the two species when analyzed over the entire campaign.

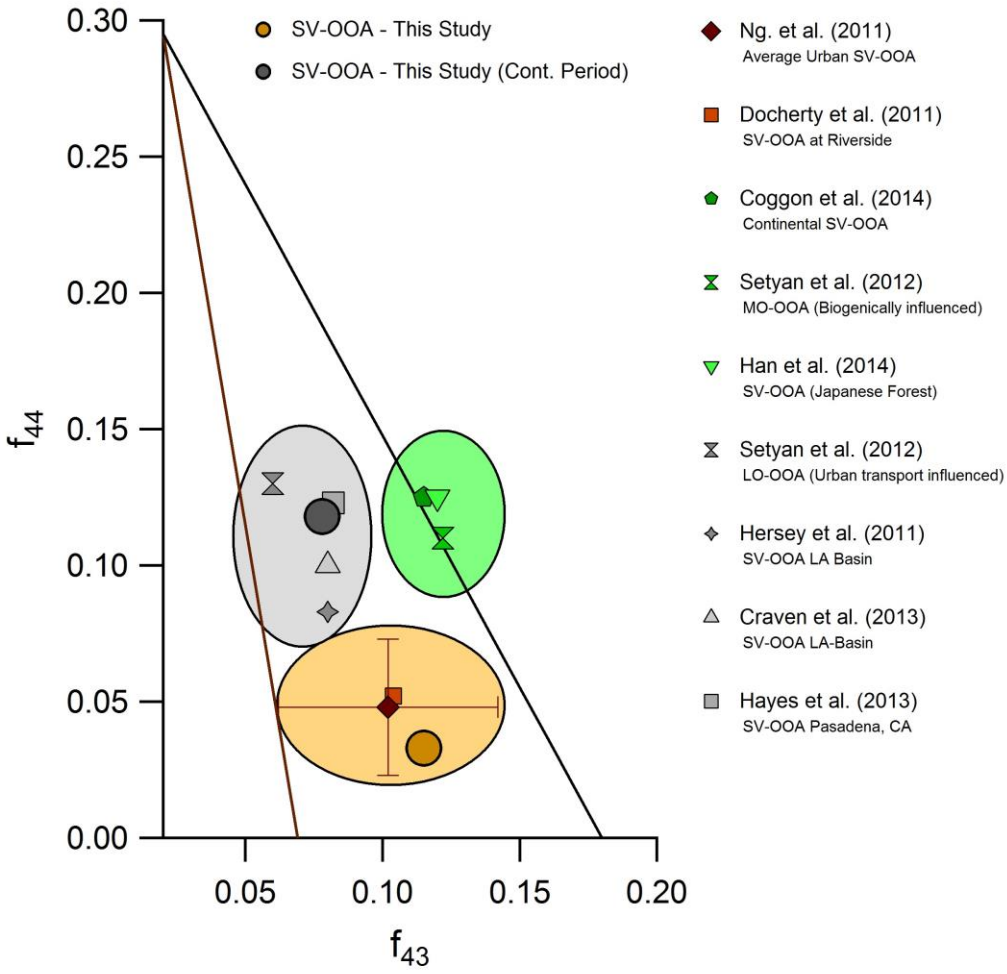

Figure S8: Comparison of the f_{44}:f_{43} ratio between SV-OOA components extracted in multiple field studies. The gray circular region represents an approximate range for anthropogenic SV-OOA, whereas the green region represents the same, but for biogenic SV-OOA, while the brown region represents a mixture of sources, based on previously apportioned SV-OOA components in the literature. When extracted from only the continental period, the SV-OOA factor falls in the anthropogenic region.

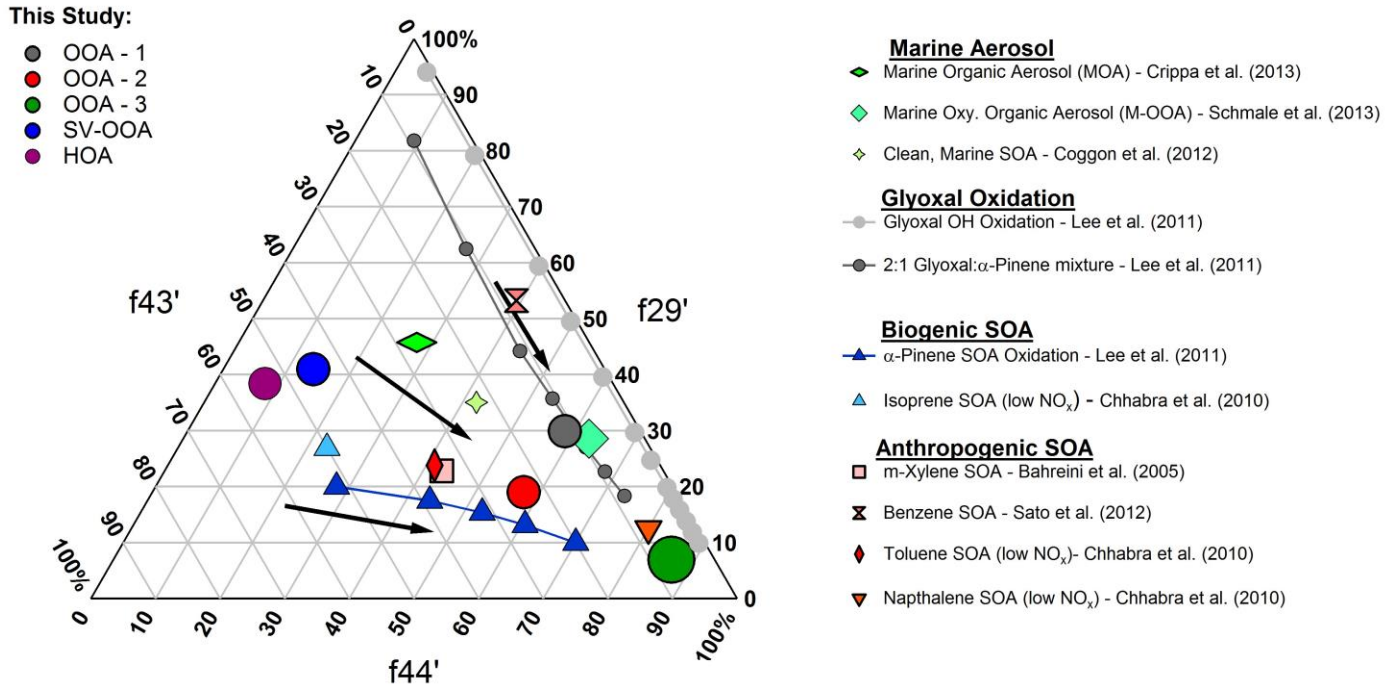

Figure S9: Ternary diagram describing relative mass fractions of m/z 29 (f29’; right), 43 (f43’; left), and 44 (f44’; bottom). PMF factors extracted from this study are depicted as large circles. Oxidation pathways of glyoxal, the 2:1 glyoxal:α-pinene ozonolysis SOA mixture, and pure α-pinene ozonolysis SOA are reproduced from Lee et al. (2011). Literature data characterizing marine aerosols are shown in green, glyoxal-related compounds are shown in gray, biogenic SOA is shown in blue, and anthropogenic SOA is shown in red. Published mass spectra for biogenic and anthropogenic SOA correspond to periods of maximum mass loading. Black arrows describe the general oxidation pathway that would be observed from various starting locations, as f29 and f43 decrease while f44 increases with oxidation (Lee et al., 2011). Note that OOA-1 falls along the oxidation pathway of the 2:1 glyoxal: α-pinene ozonolysis SOA mixture, while OOA-3 lies near the location of SOA from naphthalene, the most abundant VOC emitted by shipping vessels (Murphy et al., 2009; Czech et al., 2017).

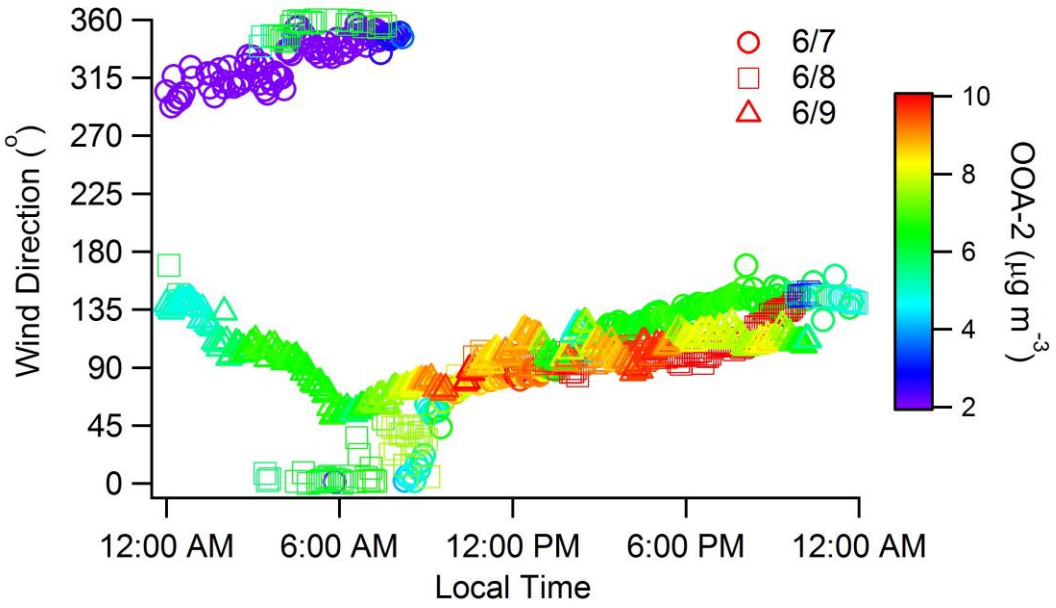

Figure S10: Variation in observed wind direction on 6/7, 6/8, and 6/9 (during the continental period). Markers are colored by the mass loading of OOA-2 to show that maximum mass loadings are observed after prevailing winds shift from offshore at night (~300^0-45^0) to primarily onshore (~90^0-135^0) midday.

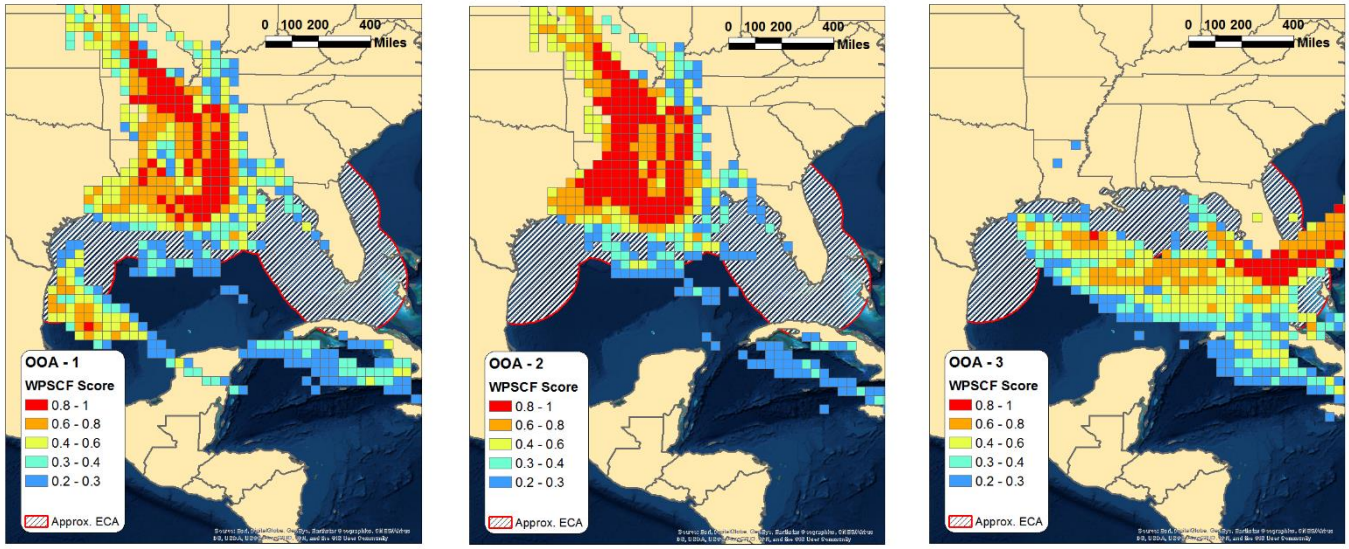

Figure S11: WPSCF plots of OOA-1 (left), OOA-2 (middle), and OOA-3 (right). The hatched region in each figure represents the approximate area encompassed by the ECA within the Gulf of Mexico (i.e. 200 nautical miles from the coastal U.S.).

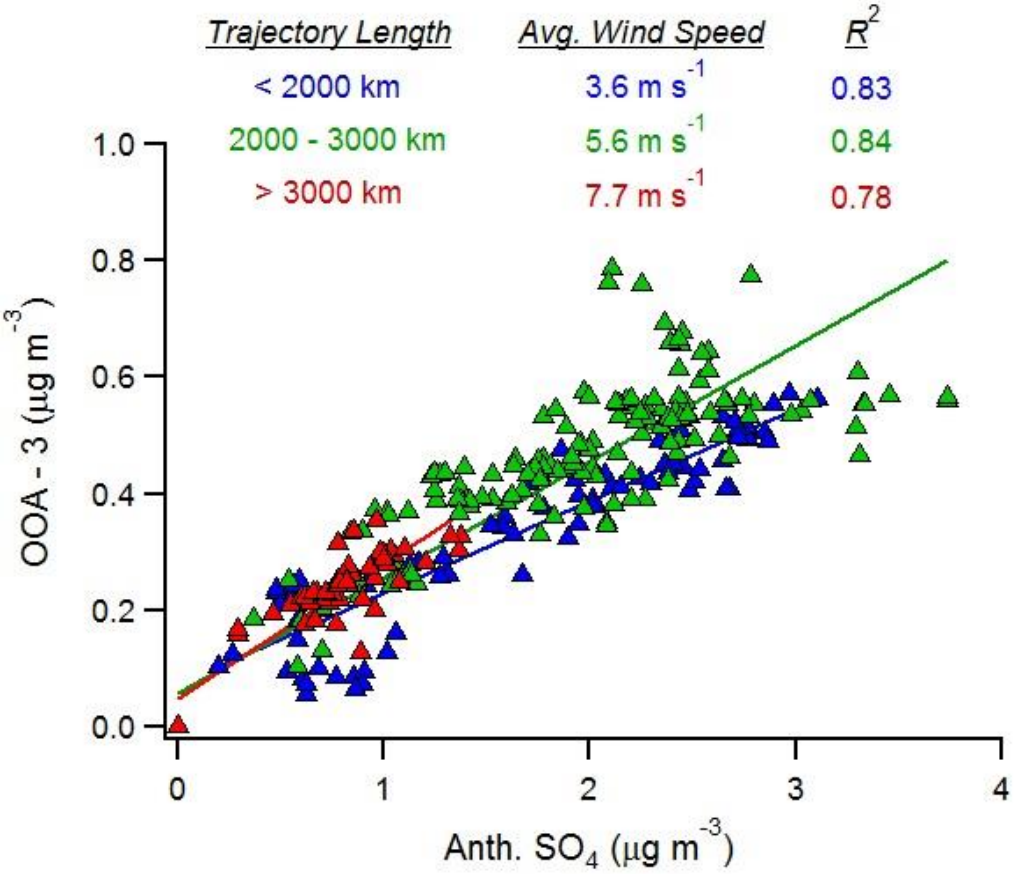

Figure S12: Correlation between hourly-averaged values of OOA-3 and anthropogenic nss-SO_4 for different ranges of trajectory-averaged wind speed.

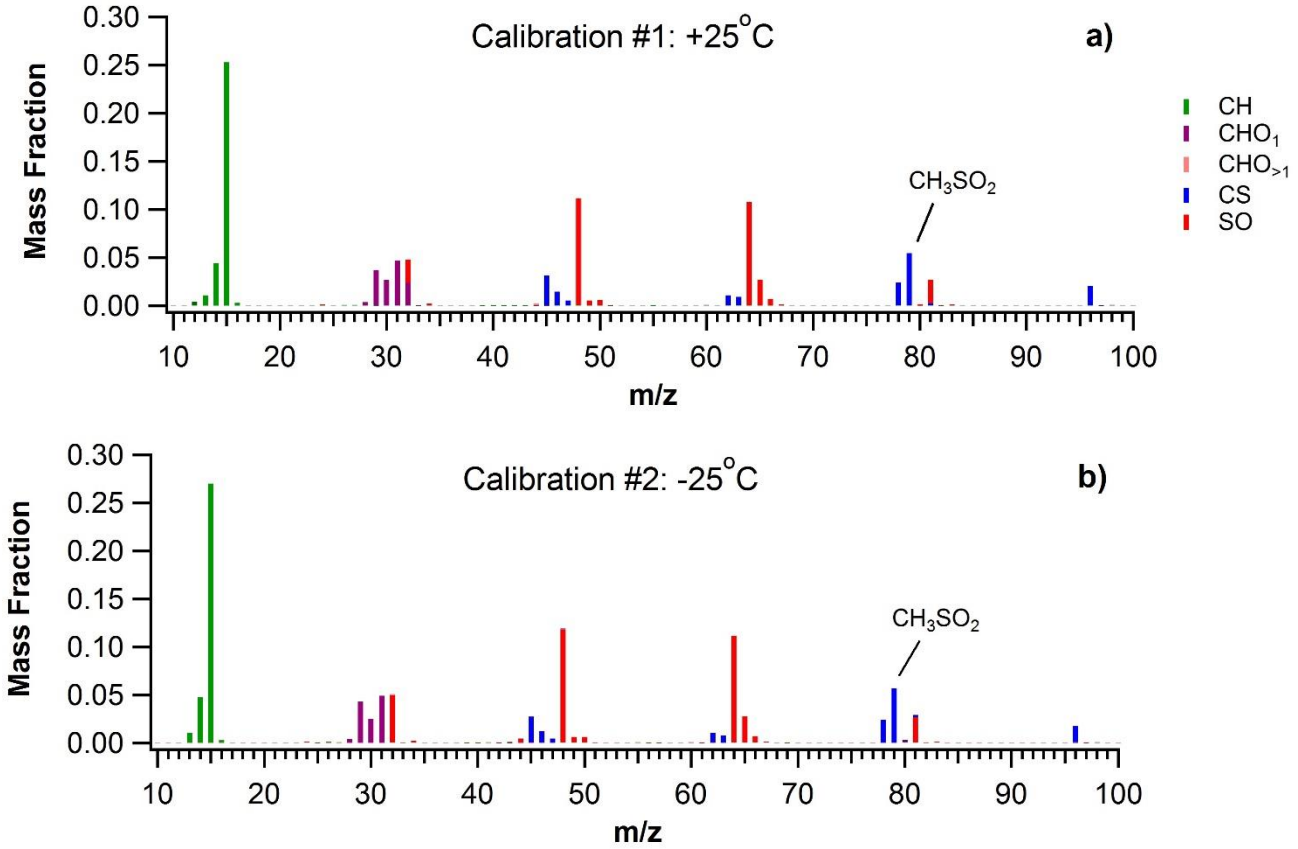

Figure S13: HR-ToF-AMS mass spectra of pure MSA (>99%) with vaporizer temperature set 25°C higher than the average during the campaign **(a)** and 25^0C lower **(b)**. The average mass fraction of $CH_3SO_2^+$ determined from the two calibrations was used to calculate MSA mass loadings.

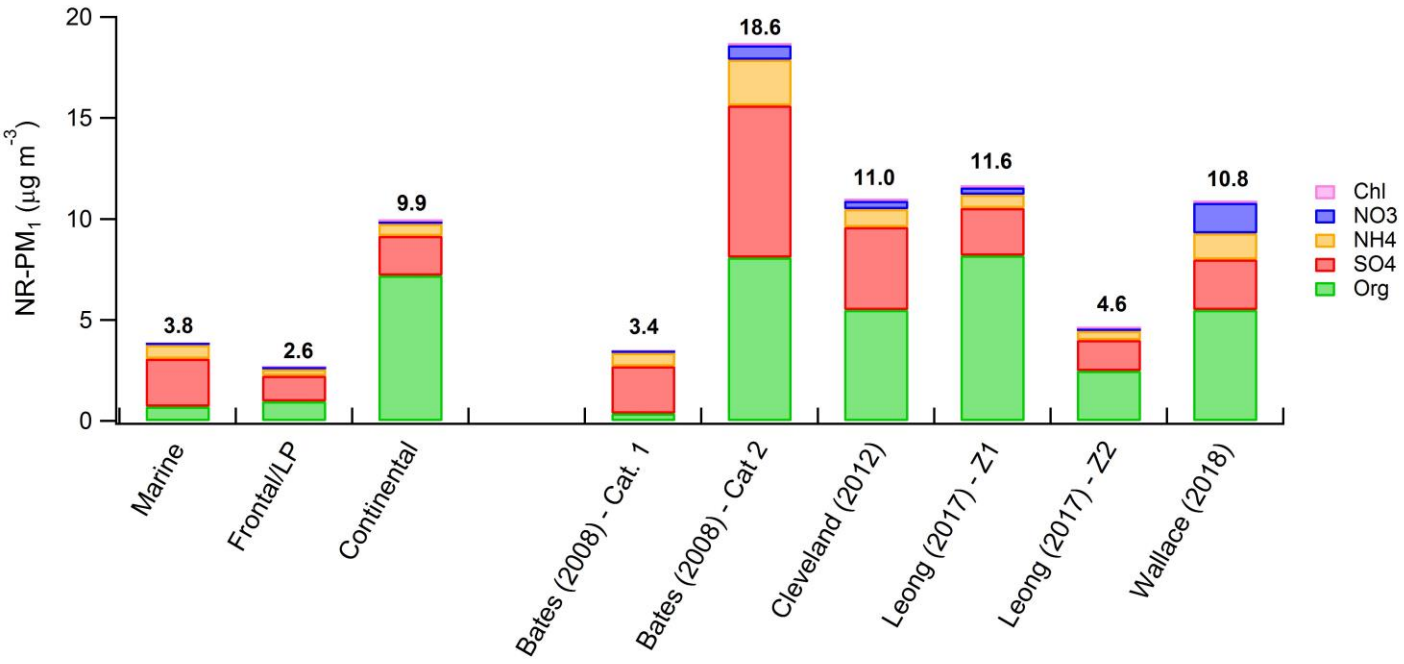

Figure S14: Comparison of average NR-PM_1 mass loadings measured during each of the three distinct periods of the campaign with previous AMS measurements near the Houston region. Values from Bates et al. (2008) are grouped into "Category 1" air masses (onshore flow) and "Category 2" air masses (offshore flow). Values from Leong et al. (2017) are grouped into average measurements in "Zone 1" (north Houston) and "Zone 2" (southeast Houston/HSC Region).

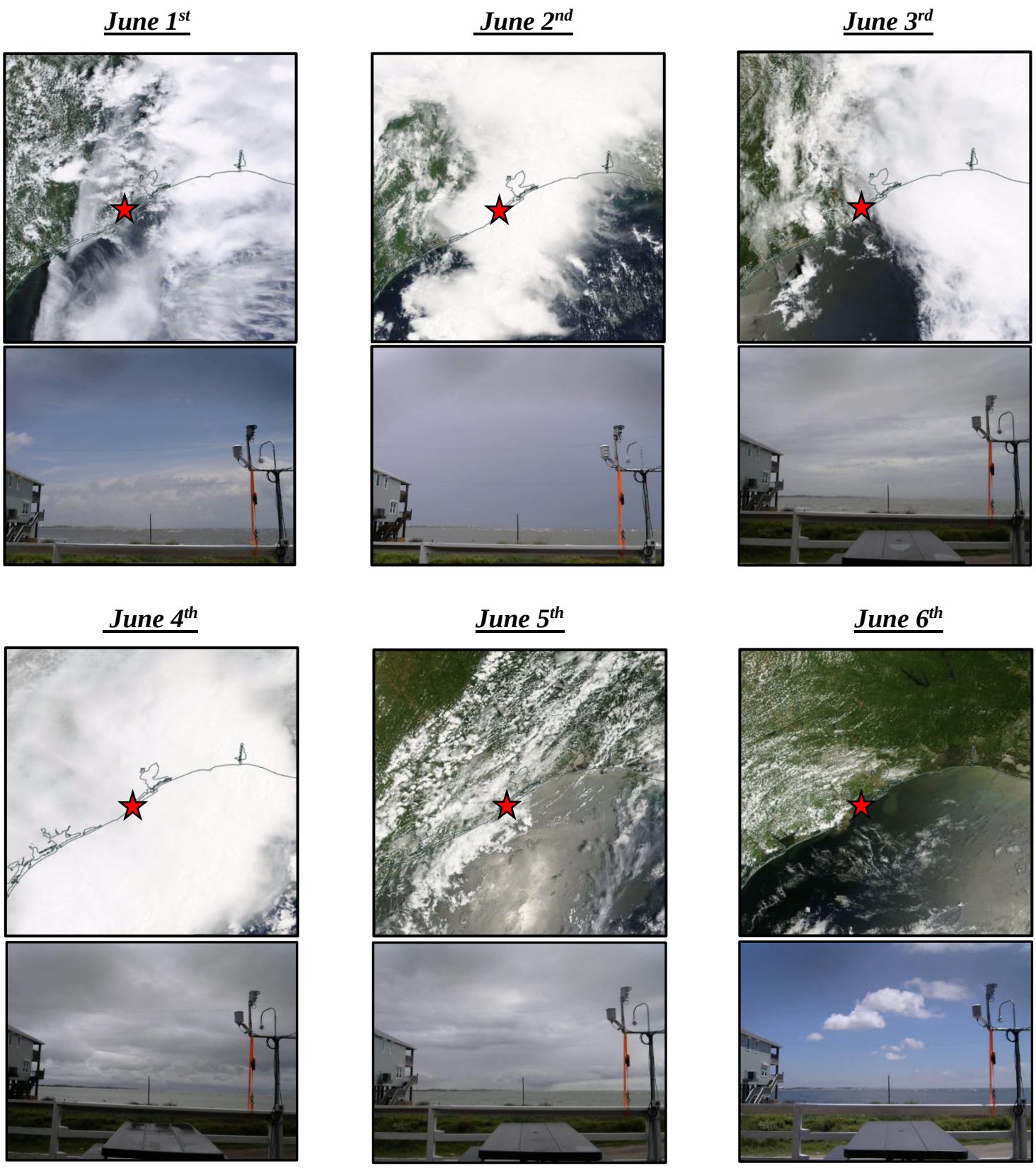

Figure S15: Imagery from NASA MODIS Satellite (https://worldview.earthdata.nasa.gov/) as well as photographs taken at 12:00 at the measurement site from 6/1 (one day prior to frontal/LP period) to 6/6 (the first day after the frontal/LP period).

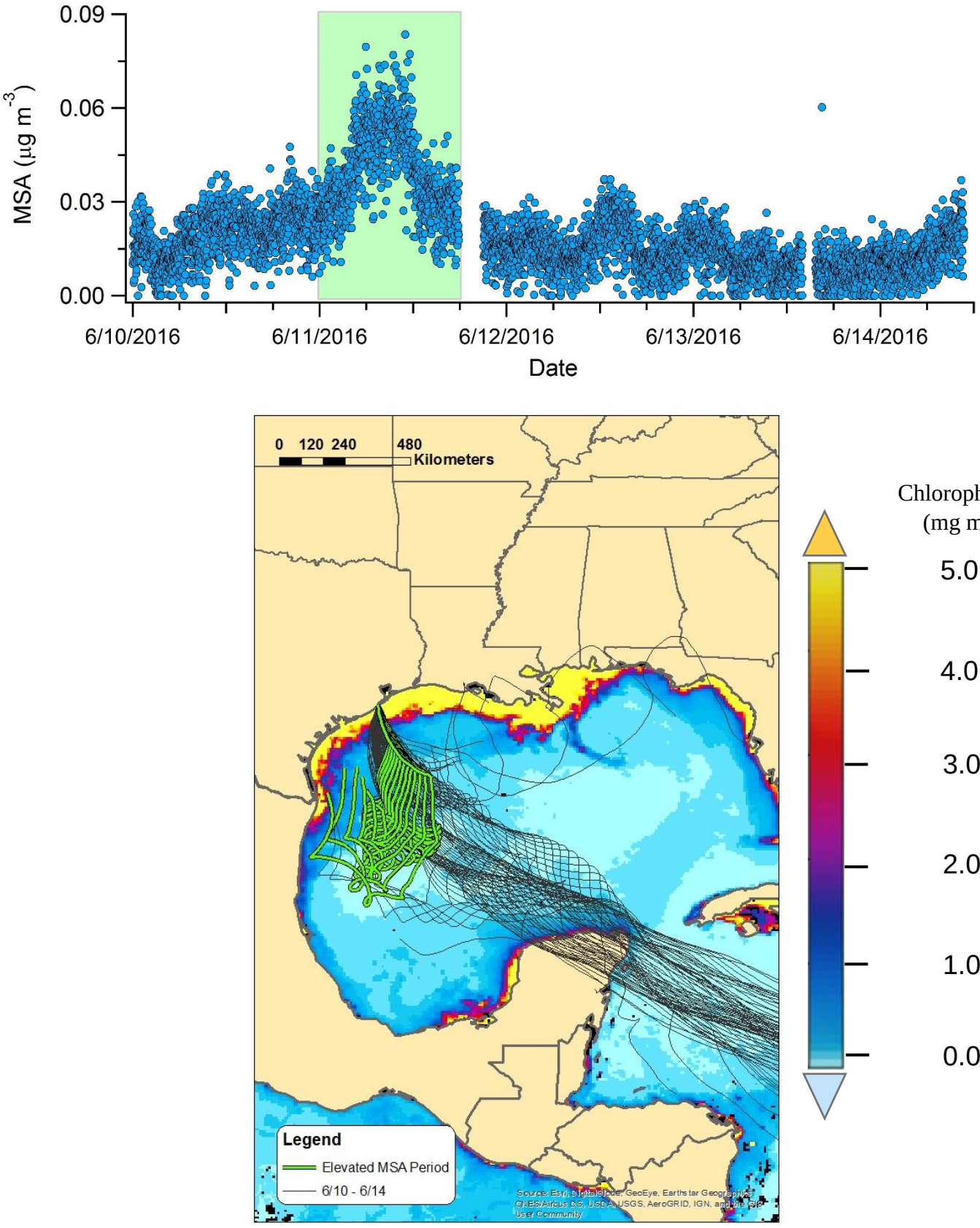

Figure S16: (Top) MSA time series (6/10 – 6/14) highlighting a period of elevated MSA mass loadings. (Bottom) Hourly five-day backward trajectories calculated from 6/10 – 6/14, with trajectories corresponding to the elevated MSA period shown in green. Average chlorophyll-a concentrations (mg m^{-3}) observed by the NASA MODIS satellite in the Gulf of Mexico are shown for reference (https://giovanni.gsfc.nasa.gov).

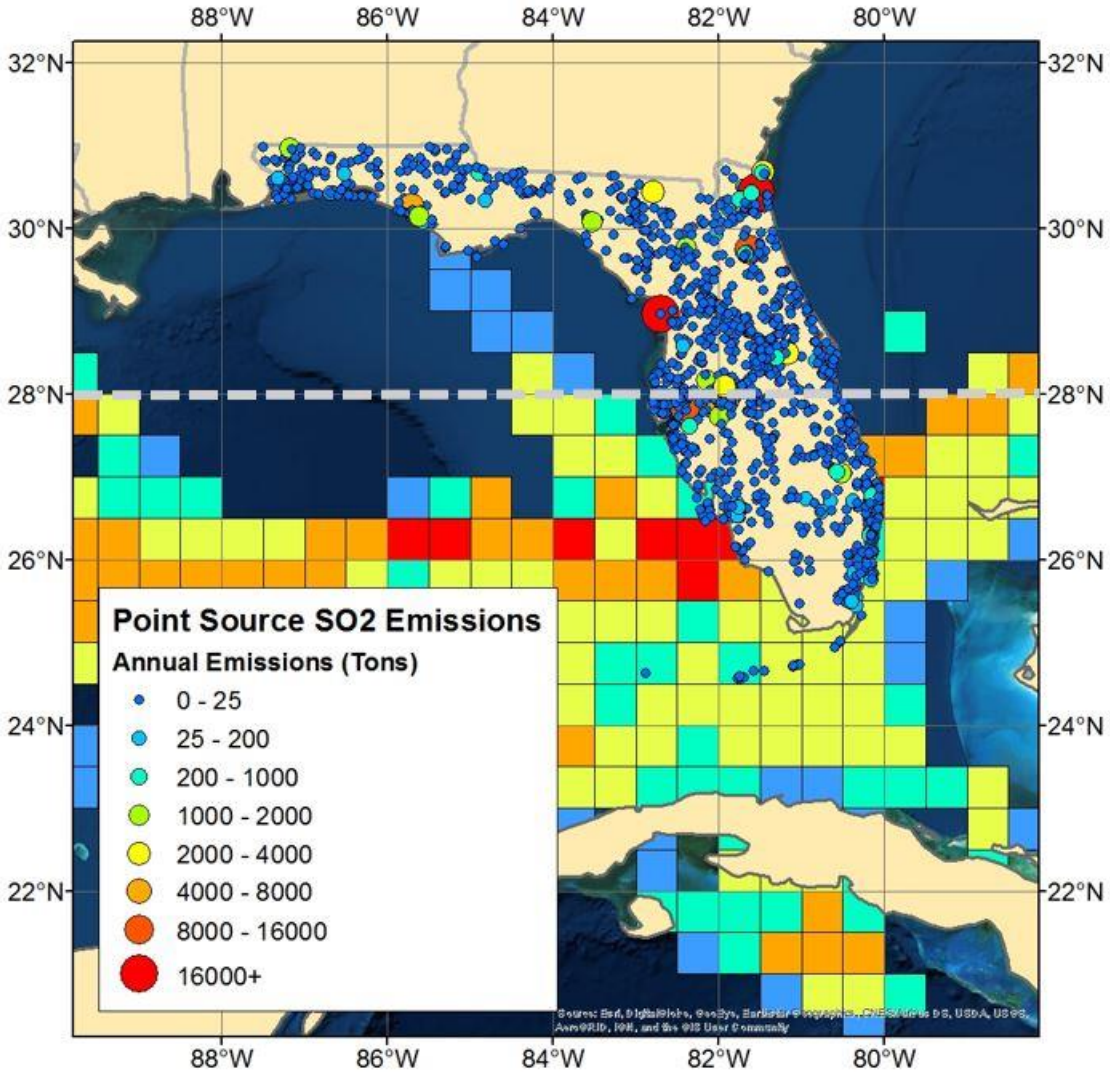

Figure S17: Depiction of SO_2 point sources in Florida according to the 2014 NEI. The WPSCF grid for anthropogenic nss-SO_4 is shown for reference. Only a small fraction of SO_2 (~19%) is emitted south of 28^{o}N latitude, highlighted with a hatched grey line.

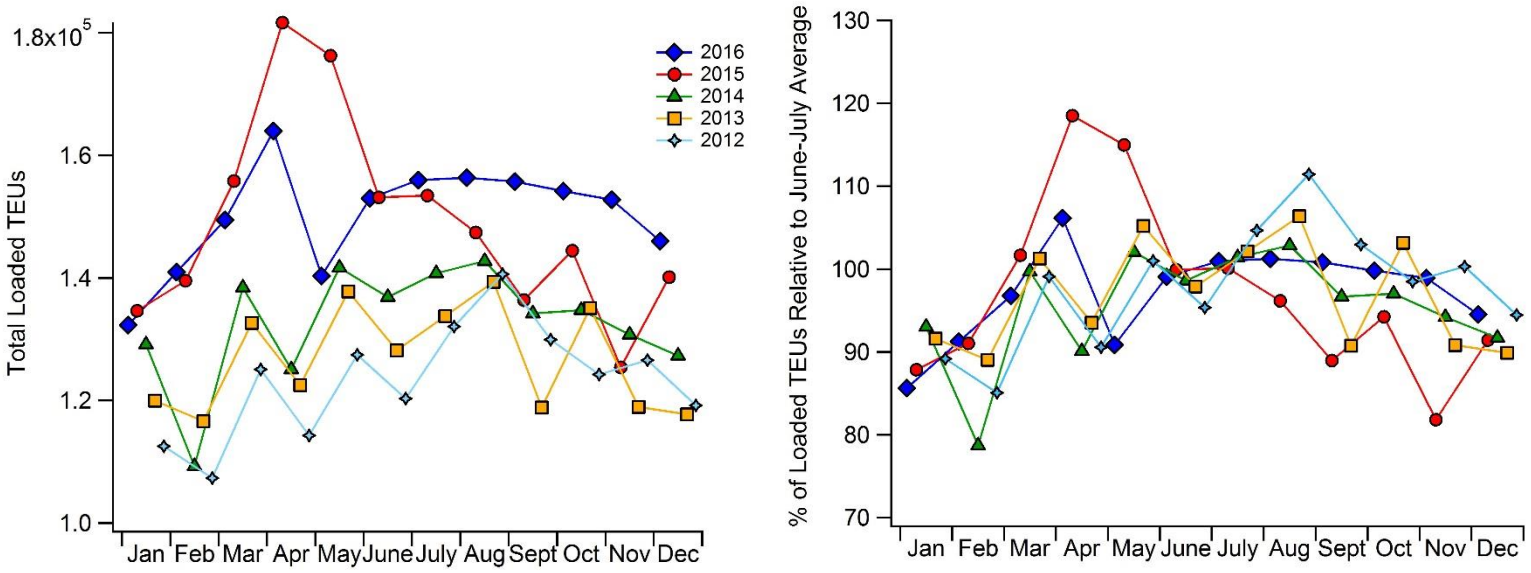

Figure S18: (Left) Total number of loaded TEUs processed per month at the Port of Houston from 2012 to 2016 (used as a proxy for the magnitude of shipping traffic). (Right) Number of TEUs processed in a specific month relative to the June-July average (%) (Port of Houston, 2017).

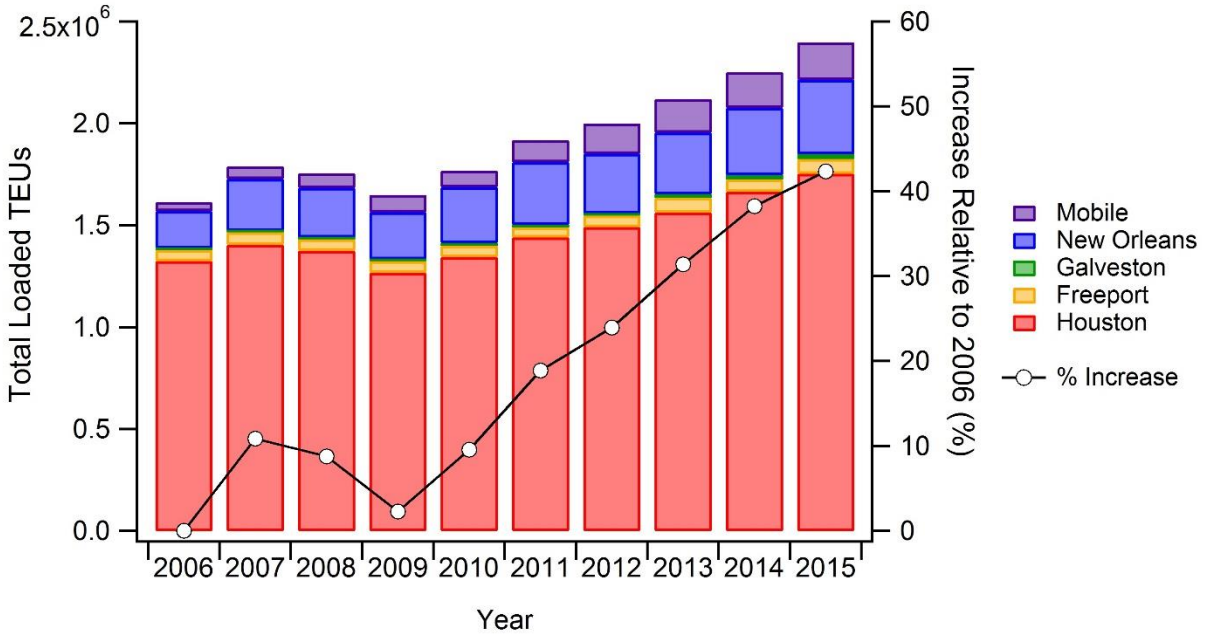

Figure S19: Annual number of TEUs loaded and unloaded at the Ports of Houston, Freeport, Galveston, New Orleans, and Mobile (left axis) as well as the cumulative percent increase since 2006 (when previous measurements by Bates et al. (2008) were performed).

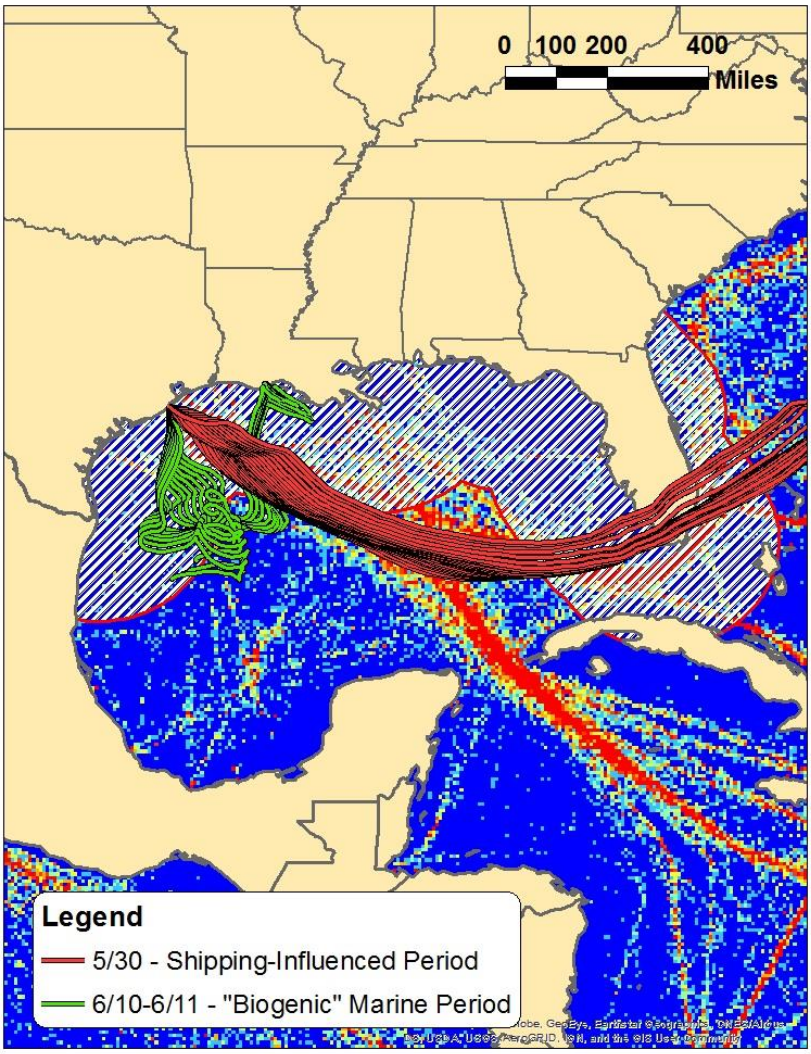

Figure S20: Five-day backward trajectories corresponding to a period heavily influenced by shipping emissions (red), and the "marine-biogenic" period (green), during which trajectories remained within the ECA for nearly their entire travel time. The hatched area represents the ECA, while colored points represent the shipping emissions allocation factor (SEAF) (red = highest density of shipping traffic).

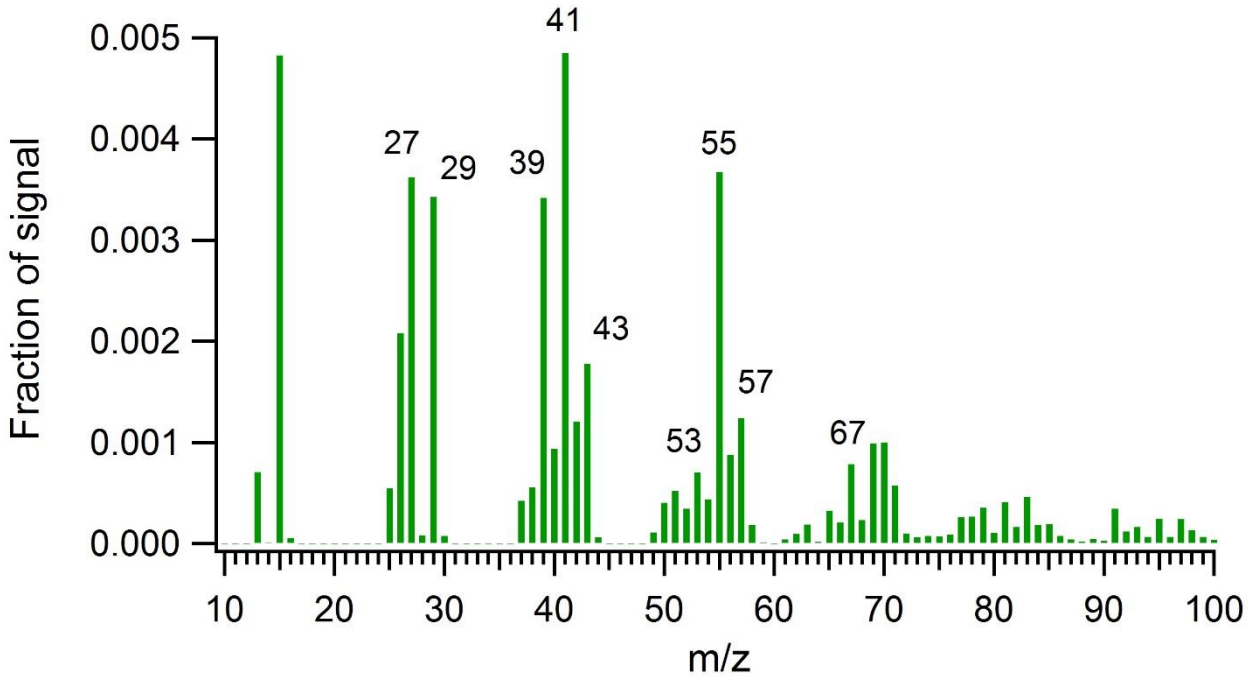

Figure S21: Mass spectra of non-oxygenated organic fragments (CH) that comprise OA during the marine-biogenic period. The prominent fragments observed are similar to the results of Ovadnevaite et al. (2011), Bates et al. (2012), and Ovadnevaite et al. (2014) for marine OA.

Model Description and Major Assumptions

Model Overview

A thorough description of the 0-D model used in this study is provided in Schulze et al. (2017). The isoprene oxidation mechanism was obtained directly from the Master Chemical Mechanism (MCM v. 3.2 via website: http://mcm.leeds.ac.uk/MCMv3.2; Jenkin et al., 1997; Saunders et al., 2003). Deposition of gas and aerosol species is assumed to occur onto a 10-m canopy layer, with resistance to deposition determined using the method of Meyers and Baldocchi (1988). As the HSC is highly urbanized with only sparse tree cover, this method will likely over-predict gas phase deposition rates and therefore lead to conservative predictions of isoprene-derived SOA production. Gas-particle partitioning of species other than glyoxal, methylglyoxal, and isoprene epoxides is based on the equilibrium model developed by Colville and Griffin (2004). Reactive uptake of glyoxal, methylglyoxal, and isoprene epoxides is assumed proportional to aerosol SA. Average diurnal isoprene, O_3, and NO_x concentrations measured by five monitors within the HSC during the marine period were used as model constraints (Figure S22). Diurnal OH concentrations were taken from measurements in downtown Houston during the SHARP 2009 campaign (Ren et al., 2013), which were approximately twice as large as average diel concentrations in the remote tropical boundary layer (Vaughan et al., 2012). While the use of previously measured OH concentrations introduces uncertainty into the calculation of absolute SOA production totals, any changes to diel OH concentrations will affect both isoprene-derived OA and AVOC-SOA, meaning relative differences in SOA production rates should not be greatly influenced. The boundary layer height of the model was assumed to vary diurnally from 100m at night to a maximum of 800m in the afternoon based on HYSPLIT modeling of transport from the coast described below.

Calculation of Aerosol SA

The average mass-based size distribution provided by the HR-ToF-AMS was utilized to calculate the aerosol SA concentration measured during the marine period. The vacuum aerodynamic diameter provided by the HR-ToF-AMS was first converted into mobility diameter by dividing by the composition-dependent average density of marine aerosol. The density of OA was assumed to be 1.4 g cm^{-3} while the assumed density of SO_4 and NH_4 was 1.78 g cm^{-3}. It was assumed that OA and SO_4/NH_4 particles were internally mixed. Aerosol liquid water was assumed to add mass to existing particles with the same fractional size distribution as SO_4, and a new radius for particles in each size bin was then calculated before determining the new SA (using the density of ALW to calculate an added volume).

Loss of Aerosol SA During Transport

Forward-trajectory HYSPLIT model runs were calculated to determine the effect of dry deposition on marine particles prior to passage over the HSC. Figure S23 highlights that on average, marine air masses

measured at 12:00 local time passed over the HSC between 3 and 5 hours later, with HYSPLIT-calculated mixing layer heights between ~550 and 1200m. Assuming a rapid submicron aerosol deposition velocity of (~0.75 cm s^{-1}) (Vong et al., 2010) and an average mixing layer height (800m), the lifetime of submicron particles with respect to dry deposition during transport is ~30 hours. With a 4-hr average travel time, dry deposition results in a ~13% loss of submicron NR-PM_1 mass during transport. Further SA loss results from the evaporation of shipping-related ALW with transport away from the coast. While the average RH was 82% at the measurement site during the marine period, the average RH measured by the HSC monitors during the marine period was 75%. For a rough estimate of the average amount of ALW lost to evaporation during transport, we modeled ALW as RH decreased (linearly) from 82% to 75% over four hours, using average marine NR-PM_1 composition. We assumed a loss of 13% of all inorganic components during the same time interval. Overall, ISORROPIA predicts 27% of ALW is lost during transport under these assumed conditions. We accounted for both deposition and evaporation in our assumed SA concentrations used for modeling aqSOA production. The effects of emissions between the coast and the HSC are not taken into account in this scenario.

Modeling AVOC-SOA

To determine representative daily AVOC-SOA production rates in the HSC, hourly gas-phase AVOC data were collected from the five HSC monitoring sites shown in Figure S22 for the marine period of the study (5/24-6/1 & 6/10-6/14). The framework introduced in Tsimpidi et al. (2010) was used to model SOA production from these species. In this mechanism, VOCs are lumped into different chemical classes based on chemical structure (Table S5; Figures S24 and S25). Using the volatility basis set (VBS) approach (Lane et al., 2008), measured VOCs are assumed to react in the gas phase to produce four different organic condensable gas species (OCGs) (Eq. S3) with yields dependent on the chemical class (Table S6) (Eq. S3). The four product species are assigned representative MWs depending on the source compounds and have different effective saturation concentrations at 298K (C^*: 1, 10, 100, and 1000 µg m^{-3}). These product species are also allowed to undergo further chemical aging following the method of Tsimipidi et al. (2010) (Eq. S5). Gas-phase reaction with OH is assumed to decrease the volatility of OCGs by one order of magnitude (e.g., transition from C^* = 1000 to C^* = 100). The aging rate constant for all species is assumed to be 1 x 10^{-11} cm^3 $molec^{-1}$ s^{-1}. A 7.5% increase in mass is included with each aging step to account for added oxygen molecules. Only OCGs in the gas phase are allowed to age. Equations S3-S6 below, adapted from Tsimpidi et al. (2010), describe this process.

$$VOC_{(g)} + OH \rightarrow \sum_{i=1}^{n} a_i OCG_{i\,(g)} \quad \text{(S3)}$$

$$OCG_{i\,(g)} \leftrightarrow OCG_{i\,(p)} \quad \text{(S4)}$$

$$OCG_{i\,(g)} + OH \rightarrow 1.075\, OCG_{i-1\,(g)} \quad \text{(S5)}$$

$$OCG_{i-1\,(g)} \leftrightarrow OCG_{i-1\,(p)} \quad \text{(S6)}$$

In the above equations, *i* represents the corresponding volatility bin of the OCG. All gas-phase OCG concentrations were assumed to be zero at the start of the model run. This method allows comparison of the potential daily production from measured AVOCs to the AMA effect. As is discussed in the main text, ~80% of total SOA predicted from this method is the result of OCG aging, in agreement with previous under-predictions of SOA from models that lacked representation of this process (Hayes et al., 2015 and references therein). Isoprene product modeling indicated high-NO_x ambient conditions in the HSC, as would be expected, so high-NO_x product yields were used (Table S6).

As the particle-phase fraction of each VBS product is a function of the background OA mass loading (Eq. S7), total predicted SOA production is subsequently highly dependent on this value.

$$f_{i,part} = (1 + \frac{C_i^*}{[OA]})^{-1} \quad \text{(S7)}$$

In equation S7, $f_{i,part}$ represents the fraction of the respective VBS product (i) in the particle phase, C_i* is the product's effective saturation concentration (μg m^{-3}), and [OA] is the ambient OA mass loading (μg m^{-3}). As ambient OA in the HSC was not quantified during the marine period of the study, conservative upper (8 μg m^{-3}) and lower (3 μg m^{-3}) estimates of ambient OA were used to produce a reasonable range of possible values. The lower limit was based on OA measurements by Leong et al. (2017) in the southern Houston region (average OA = 2.48 μg m^{-3}), while the upper limit was chosen to be larger than average OA values observed by Cleveland et al. (2012) near the HSC during more than one month of measurements (5.5 μg m^{-3}), by Bates et al. (2008) during northerly flow in and around Galveston Bay (7.45 μg m^{-3}), and during the continental period of this study (7.21 μg m^{-3}). These assumptions represent a major source of uncertainty involved in calculating the relative impact of the AMA effect, supporting the need for future large scale modeling studies that can more accurately predict ambient OA.

Figure S22: Location of TCEQ monitoring sites used for modeling HSC SOA production.

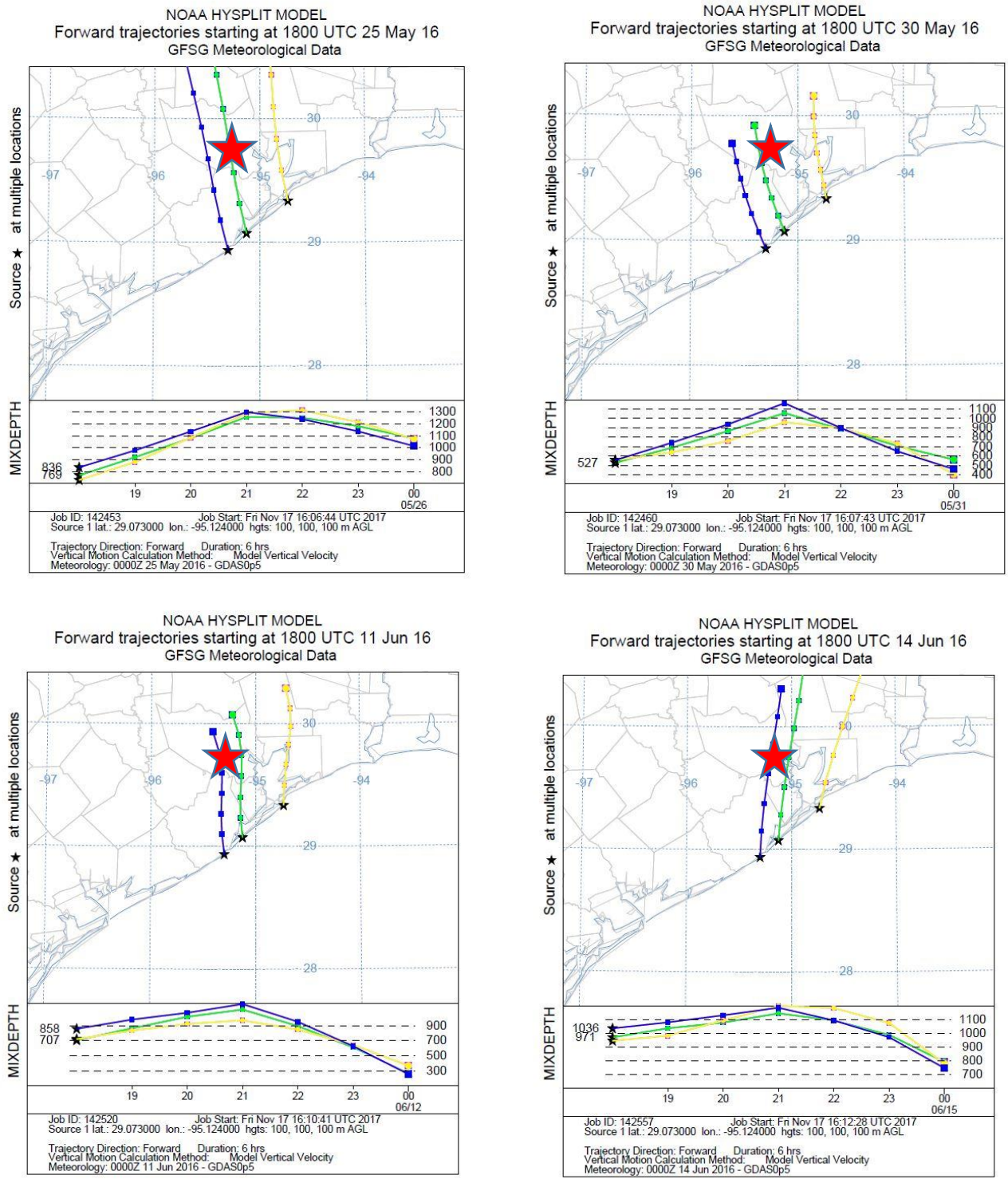

Figure S23: 6-hour HYSPLIT forward trajectories calculated at 12:00 local time for four days during the marine period. The green trajectory originates from the measurement site. Markers are spaced at 1-hr intervals. The red star represents the approximate location of the HSC. Average travel time and mixing layer depth during transport to the HSC were used to determine aerosol mass lost to deposition.

Table S5: Lumped hydrocarbon species, individual hydrocarbons within each species, and corresponding gas-phase OH reaction rate constants. Lumped species were taken from Tsimpidi et al. (2010). Reaction rate constants were obtained from Hayes et al. (2015).

Lumped Species	Hydrocarbon	k(OH) (cm^3 $molec^{-1}$ s^{-1})
ALK5	Methylcyclopentane	5.68e-12
	Cyclohexane	6.97e-12
	Methylcyclohexane	9.64e-12
	n-Heptane	6.76e-12
	2-Methylhexane	6.89e-12
	3-Methylhexane	7.17e-12
	2,3-Dimethylpentane	7.15e-12
	2,4-Dimethylpentane	7.15e-12
	n-Octane	8.11e-12
	3-Methylheptane	8.59e-12
	2-Methylheptane	8.31e-12
	2,2,4-Trimethylpentane	3.34e-12
	2,3,4-Trimethylpentane	6.60e-12
	n-Nonane	9.70e-12
	n-Decane	11.0e-12
	n-Undecane	12.3e-12
OLE1	Propene	26.3e-12
	1-Butene	31.4e-12
	1-Pentene	31.4e-12
OLE2	1,3-Butadiene	66.6e-12
	Trans-2-Pentene	67.0e-12
	Cis-2-Pentene	65.0e-12
	Styrene	58.0e-12
ARO1	Toluene	5.63e-12
	Ethylbenzene	7.00e-12
	n-Propylbenzene	6.30e-12
	Benzene	1.22e-12
ARO2	1,2,3-Trimethylbenzene	11.9e-12
	1,2,4-Trimethylbenzene	32.7e-12
	1,3,5-Trimethylbenzene	32.5e-12
	p+m-Xylene	56.7e-12
	o-Xylene	23.1e-12

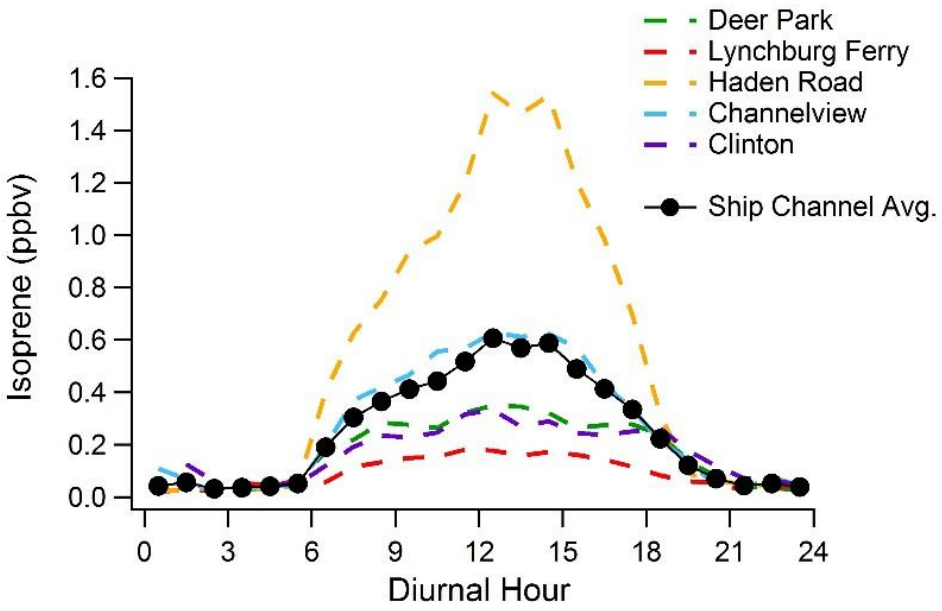

Figure S24: Diurnal concentrations of isoprene measured at five monitoring sites around the HSC during the marine period. Average diurnal profiles for each species were used to estimate local SOA production.

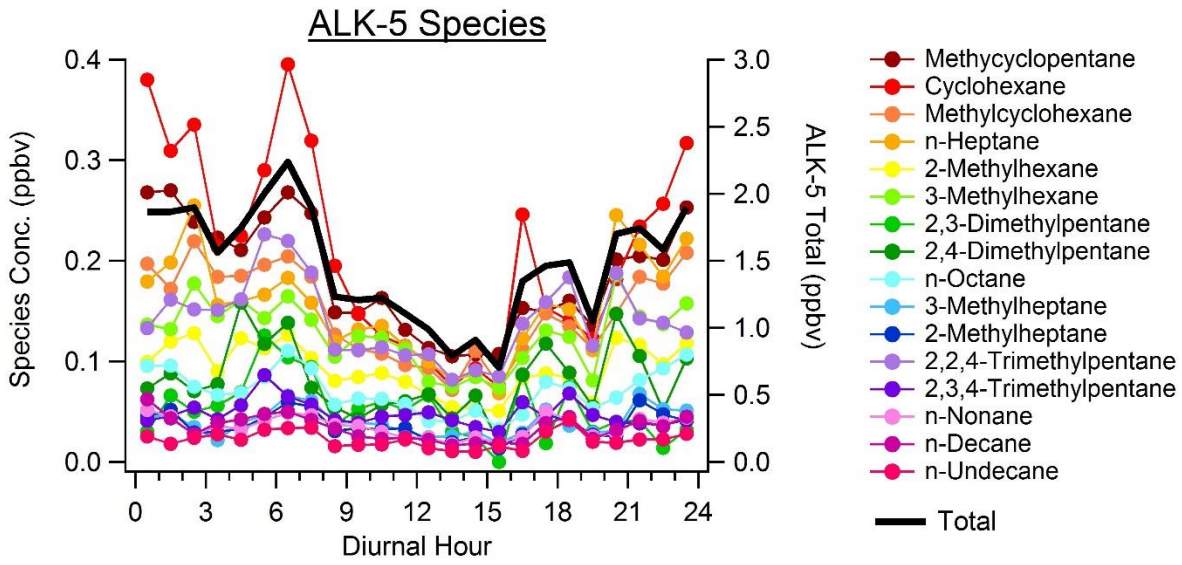
ALK-5 Species
Species Conc. (ppbv)
ALK-5 Total (ppbv)
Diurnal Hour
0.0
0.1
0.2
0.3
0.4
0.5
1.0
1.5
2.0
2.5
3.0
0
3
6
9
12
15
18
21
24
Methycyclopentane
Cyclohexane
Methylcyclohexane
n-Heptane
2-Methylhexane
3-Methylhexane
2,3-Dimethylpentane
2,4-Dimethylpentane
n-Octane
3-Methylheptane
2-Methylheptane
2,2,4-Trimethylpentane
2,3,4-Trimethylpentane
n-Nonane
n-Decane
n-Undecane
Total

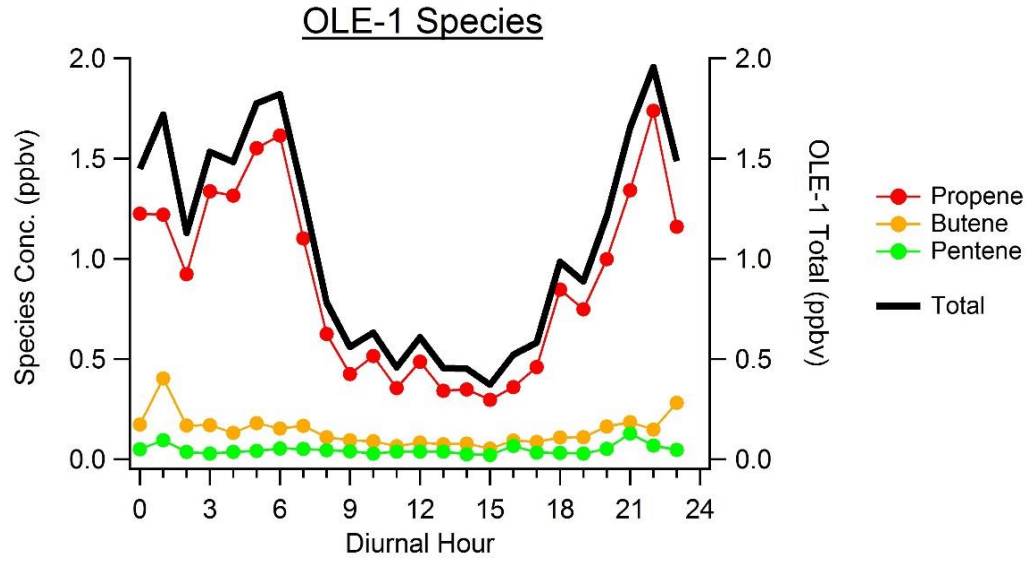
OLE-1 Species
Species Conc. (ppbv)
OLE-1 Total (ppbv)
Diurnal Hour
0.0
0.5
1.0
1.5
2.0
0
3
6
9
12
15
18
21
24
Propene
Butene
Pentene
Total

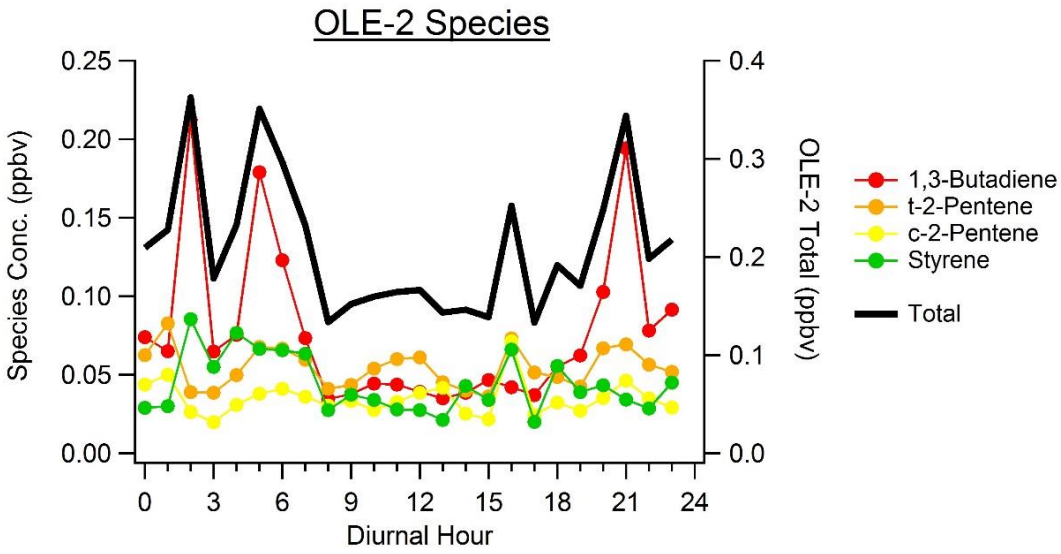
OLE-2 Species
Species Conc. (ppbv)
OLE-2 Total (ppbv)
Diurnal Hour
0.00
0.05
0.10
0.15
0.20
0.25
0.0
0.1
0.2
0.3
0.4
0
3
6
9
12
15
18
21
24
1,3-Butadiene
t-2-Pentene
c-2-Pentene
Styrene
Total

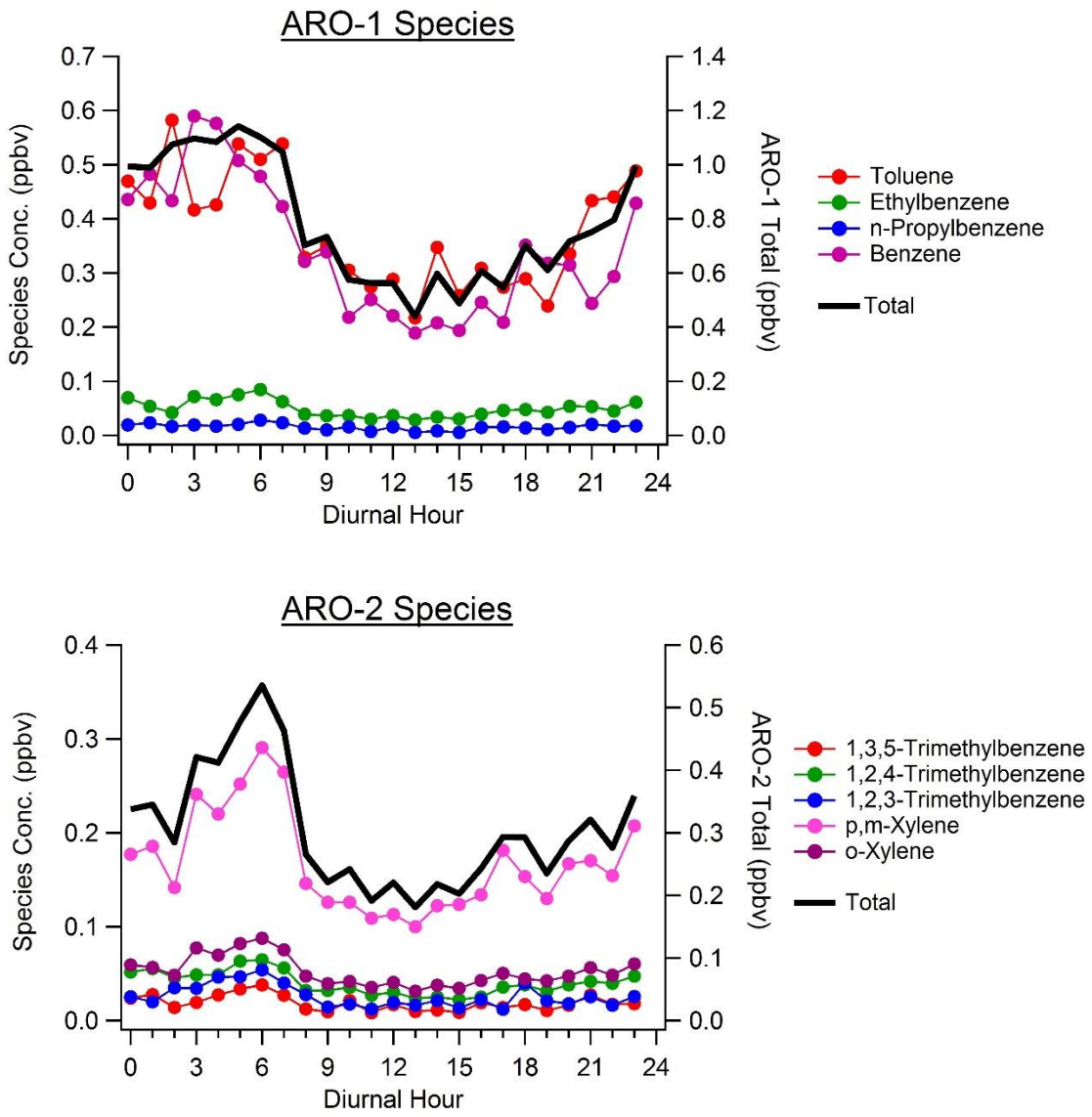

Figure S25: Diurnal concentrations (ppbv) of all gas phase AVOCs used for AVOC SOA modeling. Each graph contains all VOCs within each lumped family. Black lines denote the total concentration of each family.

Table S6: Four-product volatility basis set parameters for each lumped species.

Lumped Species	SOA Product Yield (High-NO_x Conditions)				Assumed MW (g mol^{-1})
	C* = 1 µg m^{-3}	C* = 10 µg m^{-3}	C* = 100 µg m^{-3}	C* = 1000 µg m^{-3}	
ALK5	0.000	0.015	0.000	0.000	150
OLE1	0.001	0.005	0.038	0.150	120
OLE2	0.003	0.026	0.083	0.270	120
ARO1	0.003	0.165	0.300	0.435	150
ARO2	0.002	0.195	0.300	0.435	150

References:

1) Aiken, A. C., Salcedo, D., Cubison, M. J., Huffman, J. A., DeCarlo, P. F., Ulbrich, I. M., Docherty, K. S., Sueper, D., Kimmel, J. R., Worsnop, D. R., Trimborn, A., Northway, M., Stone, E. A., Schauer, J. J., Volkamer, R. M., Fortner, E., de Foy, B., Wang, J., Laskin, A., Shutthanandan, V., Zheng, J., Zhang, R., Gaffney, J., Marley, N. A., Paredes-Miranda, G., Arnott, W. P., Molina, L. T., Sosa, G., and Jimenez, J. L.: Mexico City aerosol analysis during MILAGRO using high resolution aerosol mass spectrometry at the urban supersite (T0) – Part 1: Fine particle composition and organic source apportionment, Atmos. Chem. Phys., 9, 6633–6653, doi: 10.5194/acp-9-6633-2009, 2009.

2) Bahreini, R., Keywood, M. D., Ng, N. L., Varutbangjul, V., Gao, S., Flagan, R. C., Seinfeld, J. H., Worsnop, D. R., and Jimenez, J. L.: Measurements of secondary organic aerosol from oxidation of cycloalkenes, terpenes, and m-xylene using an aerodyne aerosol mass spectrometer, Environ. Sci. Technol., 39, 5674-5688, doi: 10.1021/es048061a, 2005.

3) Bates, T.S., Quinn, P.K., Coffman, D., Schulz, K., Covert, D.S., Johnson, J.E., Williams, E.J., Lerner, B.M., Angevine, W.M., Tucker, S.C., Brewer, W.A., and Stohl, A.: Boundary layer aerosol chemistry during TexAQS/GoMACCS 2006: Insights into aerosol sources and transformation processes. J. Geophys. Res-Atmos., 113, 18, doi: 10.1029/2008JD010023, 2008.

4) Bates, T. S., Quinn, P. K., Frossard, A. A., Russell, L. M., Hakala J., Petaj¨ a, T., Kulmala, M., Covert, D. S., Cappa, C. D., Li, ¨ S.-M., Hayden, K. L., Nuaaman, I., McLaren, R., Massoli, P., Canagaratna, M. R, Onasch, T. B., Sueper, D., Worsnop, D. R., and Keene, W. C.: Measurements of ocean derived aerosol off the coast of California, J. Geophys. Res., 117, D00V15, doi: 10.1029/2012JD017588, 2012.

5) Bean, J. K., Faxon, C. B., Leong, Y. J., Wallace, H. W., Cevik, B. K., Ortiz, S., Canagaratna, M. R., Usenko, S., Sheeshley, R. J., Griffin, R. J., and Hildebrandt, L: Composition and sources of particulate matter measured near Houston, TX; Anthropogenic-biogenic interactions, Atmos., 5, 73, doi: 10.3390/atmos7050073, 2016.

6) Canagaratna, M. R., Jayne, J. T., Ghertner, D. A., Herndon, S., Shi, Q., Jimenez, J. L., Silva, P. J., Williams, P., Lanni, T., Drewnick, F., Demerjian, K. L., Kolb, C. E., and Worsnop, D. R.: Chase studies of particulate emissions from in-use New York City vehicles, Aerosol Sci. Tech., 38, 555-573, doi: 10.1080/02786820490465504, 2004.

7) Chang, R. Y.-W., Leck, C., Graus, M., Müller, M., Paatero, J., Burkhart, J. F., Stohl, A., Orr, L. H., Hayden, K., Li, S.-M., Hansel, A., Tjernström, M., Leaitch, W. R., and Abbatt, J. P. D.: Aerosol composition and sources in the central Arctic Ocean during ASCOS, Atmos. Chem. Phys., 11, 10619–10636, doi: 10.5194/acp-11-10619-2011, 2011.

8) Chen, Q., Farmer, D. K., Rizzo, L. V., Pauliquevis, T., Kuwata, M., Karl, T. G., Guenther, A., Allan, J. D., Coe, H., Andreae, M. O., Pöschl, U., Jimenez, J. L., Artaxo, P., and Martin, S. T.: Submicron particle mass concentrations and sources in the Amazonian wet season (AMAZE-08), Atmos. Chem. Phys., 15, 3687-3701, doi: 10.5194/acp-15-3687-2015, 2015.

9) Chhabra, P. S., Flagan, R. C., and Seinfeld, J. H.: Elemental analysis of chamber organic aerosol using an aerodyne high-resolution aerosol mass spectrometer, Atmos. Chem. Phys., 10, 4111–4131, doi: 10.5194/acp-10-4111-2010, 2010.

10) Cleveland, M. J., Ziemba, L. D., Griffin, R. J., Dibb, J. E., Anderson C. H., Lefer, B., and Rappengluck, B.: Characterization of urban aerosol using aerosol mass spectrometry and proton nuclear magnetic resonance spectroscopy, Atmos. Environ., 54, 511-518, doi: 10.1016/j.atmosenv.2012.02.074, 2012.

11) Colville, C. J. and Griffin, R. J.: The roles of individual oxidants in secondary organic aerosol formation from 13-carene: 2. SOA formation and oxidant contribution, Atmos. Environ., 38, 4013– 4023, doi: 10.1016/j.atmosenv.2004.03.063, 2004.

12) Coggon, M.M., Sorooshian, A., Wang, Z., Craven, J.S., Metcalf, A.R., Lin, J.J., Nenes, A., Jonsson, H.H., Flagan, R.C., and Seinfeld, J.H.: Observations of continental biogenic impacts on marine aerosol and clouds off the coast of California. J. Geophys. Res., 119, 6724-6748, doi: 10.1002/2013JD021228, 2014.

13) Coggon, M. M., Sorooshian, A., Wang, Z., Metcalf, A. R., Frossard, A. A., Lin, J. J., Craven, J. S., Nenes, A., Jonsson, H. H., Russell, L. M., Flagan, R. C., and Seinfeld, J. H.: Ship impacts on the marine atmosphere: insights into the contribution of shipping emissions to the properties of marine aerosol and clouds, Atmos. Chem. Phys., 12, 8439–8458, doi: 10.5194/acp-12-8439- 2012, 2012.

14) Craven, J. S., Metcalf, A. R., Bahreini, R., Middlebrook, A., Hayes, P. L., Duong, H. T., Sorooshian, A., Jimenez, J. L., Flagan, R. C., and Seinfeld, J. H.: Los Angeles Basin airborne organic aerosol characterization during CalNex, J. Geophys. Res.-Atmos., 118, 11453–11467, doi: 1-.1002/jgrd.50853, 2013.

15) Crippa, M., El Haddad, I., Slowik, J. G., DeCarlo, P. F., Mohr, C., Heringa, M. F., Chirico, R., Marchand, N., Sciare, J., Baltensperger, U., and Prévôt, A. S. H.: Identification of marine and continental aerosol sources in Paris using high resolution aerosol mass spectrometry, J. Geophys. Res.-Atmos., 118, 1950–1963, doi: 10.1002/jgrd.50151, 2013.

16) Czech, H., Stengel, B., Adam, T., Sklorz, M., Streibel, T., and Zimmerman, R.: A chemometric investigation of aromatic emission profiles from a marine engine in comparison with residential wood combustion and road traffic: Implications for source apportionment inside and outside sulphur emission control areas, Atmos. Env., 167, 212-222, dx.doi.org/10.1016/j.atmosenv.2017.08.022, 2017.

17) Diesch, J.-M., Drewnick, F., Klimach, T., and Borrmann, S.: Investigation of gaseous and particulate emissions from various marine vessel types measured on the banks of the Elbe in Northern Germany, Atmos. Chem. Phys., 13, 3603–3618, doi: 10.5194/acp-13-3603-2013, 2013.

18) Docherty, K. S., Aiken, A. C., Huffman, J. A., Ulbrich, I. M., De- Carlo, P. F., Sueper, D., Worsnop, D. R., Snyder, D. C., Peltier, R. E., Weber, R. J., Grover, B. D., Eatough, D. J., Williams, B. J., Goldstein, A. H., Ziemann, P. J., and Jimenez, J. L.: The 2005 Study of Organic Aerosols at Riverside (SOAR-1): Instrumental intercomparisons and fine particle composition, Atmos. Chem. Phys., 11, 12387–12420, doi: 10.5194/acp-11-12387-2011, 2011.

19) Faust, J. A., Wong, J. P. S., Lee, A. K. Y., and Abbatt, J. P. D.: Role of aerosol liquid water in secondary organic aerosol formation from volatile organic compounds, Environ. Sci. Technol, 51, 1405−1413, doi: 10.1021/acs.est.6b04700, 2017.

20) Frossard, A. A., Russell, L. M., Burrows, S. M., Elliott, S. M., Bates, T. S., and Quinn, P. K.: Sources and composition of submicron organic mass in marine aerosol particles, J. Geophys. Res.- Atmos., 119, 12977–13003, doi: 10.1002/2014JD021913, 2014.

21) Haman, C.L., Couzo, E., Flynn, J.H., Vizuete, W., Heffron, B., Lefer, B.L.: Relationship between boundary layer heights and growth rates with ground-level ozone in Houston, Texas. J. Geophys. Res.-Atmos., 119, 6230–6245. http://dx.doi.org/10.1002/2013JD020473, 2014.

22) Han, Y., Iwamoto, Y., Nakayama, T., Kawamura, K., and Mochida, M.: Formation and evolution of biogenic secondary organic aerosol over a forest site in Japan, J. Geophys. Res.-Atmos., 119, 1, 259-273, doi: 10.1002/2013JD020390, 2014.

23) Hayes, P. L., Carlton, A. G., Baker, K. R., Ahmadov, R., Washenfelder, R. A., Alvarez, S., Rappenglück, B., Gilman, J. B., Kuster, W. C., de Gouw, J. A., Zotter, P., Prévôt, A. S. H., Szidat, S., Kleindienst, T. E., Offenberg, J. H., Ma, P. K., and Jimenez, J. L.: Modeling the formation and aging of secondary organic aerosols in Los Angeles during CalNex 2010, Atmos. Chem. Phys., 15, 5773-5801, https://doi.org/10.5194/acp-15-5773-2015, 2015.

24) Hayes, P. L., Ortega, A. M., Cubison, M. J., Froyd, K. D., Zhao, Y., Cliff, S. S., Hu, W. W., Toohey, D. W., Flynn, J. H., Lefer, B. L., Grossberg, N., Alvarez, S., Rappenglück, B., Taylor, J. W., Allan, J. D., Holloway, J. S., Gilman, J. B., Kuster, W. C., de Gouw, J. A., Massoli, P., Zhang, X., Liu, J., Weber, R. J., Corrigan, A. L., Russell, L. M., Isaacman, G., Worton, D. R., Kreisberg, N. M., Goldstein, A. H., Thalman, R., Waxman, E. M., Volkamer, R., Lin, Y. H., Surratt, J. D., Kleindienst, T. E., Offenberg, J. H., Dusanter, S., Griffith, S., Stevens, P. S., Brioude, J., Angevine, W. M., and Jimenez, J. L.: Organic aerosol composition and sources in Pasadena, California, during the 2010 CalNex campaign, J. Geophys. Res.-Atmos., 118, 9233–9257, doi: 10.1002/jgrd.50530, 2013.

25) Hersey, S. P., J. S. Craven, K. A. Schilling, A. R. Metcalf, A. Sorooshian, M. N. Chan, R. C. Flagan, and J. H. Seinfeld: The Pasadena Aerosol Characterization Observatory (PACO): Chemical and physical analysis of the Western Los Angeles Basin aerosol, Atmos. Chem. Phys., 11, 7417–7443, doi: 10.5194/acp-11-7417-2011, 2011.

26) Jenkin, M. E., Saunders, S. M., and Pilling, M. J.: The tropospheric degradation of volatile organic compounds: a protocol for mechanism development, Atmos. Environ., 31, 81–104, doi: 10.1016/S1352-2310(96)00105-7, 1997.

27) Jia, L. and Xu, Y.: Effects of relative humidity on ozone and secondary organic aerosol formation from the photooxidation of benzene and ethylbenzene, Aer. Sci. Tech., 48, 1-12, doi: 10.1080/02786826.2013.847269, 2014.

28) Lack, D. A., Cappa, C. D., Langridge, J., Bahreni, R., Buffaloe, G., Brock, C. A., Cerully, K., Hayden, K., Holloway, J. S., Lerner, B., Li, S. M., McLaren, R., Middlebrook, A., Moore, R., Nenes, A., Nuaanman, I., Peischl, J., Perring, A., Quinn, P. K., Ryerson, T. B., Schwarz, J. P., Spackman, J. R., and Williams, E. J.: Impact of fuel quality regulation and speed reductions on shipping emissions: Implications for climate and air quality, Environ. Sci. Technol., 45, 9052–9060, doi: 10.1021/es2013424, 2011.

29) Lane, T. E., Donahue, N. M., and Pandis, S. N.: Simulating secondary organic aerosol formation using the volatility basis set approach in a chemical transport model, Atmos. Environ., 42, 7439–7451, doi: 10.1016/j.atmosenv.2008.06.06, 2008.

30) Lanz, V. A., Alfarra, M. R., Baltensperger, U., Buchmann, B., Hueglin, C., and Prévôt, A. S. H.: Source apportionment of submicron organic aerosols at an urban site by factor analytical modelling of aerosol mass spectra, Atmos. Chem. Phys., 7, 1503-1522, doi: 10.5194/acp-7-1503-2007, 2007.

31) Lee, A. K. Y., Herckes, P., Leaitch, W. R., Macdonald, A. M., and Abbatt, J. P. D.: Aqueous OH oxidation of ambient organic aerosol and cloud water organics: formation of highly oxidized products, Geophys. Res. Lett., 38, L11805, doi: 10.1029/2011GL047439, 2011.

32) Leong, Y. J., Sanchez, N. P., Wallace, H. W., Cevik, K., Hernandez, C. S., Han, Y., Flynn, J. H., Massoli, P., Floerchinger, C., Fortner E. C., Herndon, S., Bean, J. K., Hildebrandt Ruiz, L., Jeon, W., Choi, Y., Lefer, B., and Griffin, R. J.: Overview of surface measurements and spatial characterization of submicrometer particulate matter during the DISCOVER-AQ 2013 campaign in Houston, J. Air Waste Manag. Assoc., 28, 1-19, doi: 10.1080/10962247.2017.1296502, 2017.

33) Meyers, T. P. and Baldocchi, D. D.: A comparison of models for deriving dry deposition fluxes of O_3 and SO_2 to a forest canopy, Tellus B, 40, 270–284, doi: 10.1111/j.1600-0889.1988.tb00297.x, 1988.

34) Mohr, C., Huffman, J. A., Cubison, M. J., Aiken, A. C., Docherty, K. S., Kimmel, J. R., Ulbrich, I. M., Hannigan, M. P., and Jimenez, J. L.: Characterization of primary organic aerosol emissions from meat cooking, trash burning, and motor vehicles with high-resolution aerosol mass spectrometry and comparison with ambient and chamber observations, Environ. Sci. Technol., 43, 2443–2449, doi: 10.1021/es8011518, 2009.

35) Mohr, C., DeCarlo, P. F., Heringa, M. F., Chirico, R., Slowik, J. G., Richter, R., Reche, C., Alastuey, A., Querol, X., Seco, R., Peñuelas, J., Jiménez, J. L., Crippa, M., Zimmermann, R., Baltensperger, U., and Prévôt, A. S. H.: Identification and quantification of organic aerosol from cooking and other sources in Barcelona using aerosol mass spectrometer data, Atmos. Chem. Phys., 12, 1649-1665, https://doi.org/10.5194/acp-12-1649-2012, 2012.

36) Murphy, S. M., Agrawal, H., Sorooshian, A., Padro, L. T., Gates, H., Hersey, S., Welch, W. A., Jung, H., Miller, J. W., Cocker, D. R., Nenes, A., Jonsson, H. H., Flagan, R. C., and Seinfeld, J. H.: Comprehensive simultaneous shipboard and airborne characterization of exhaust from a modern container ship at sea, Environ. Sci. Technol., 43, 4626–4640, doi: 10.1021/es802413j, 2009.

37) Ng, N. L., Canagaratna, M. R., Jimenez, J. L., Chhabra, P. S., Seinfeld, J. H., and Worsnop, D. R.: Changes in organic aerosol composition with aging inferred from aerosol mass spectra, Atmos. Chem. Phys., 11, 6465–6474, doi: 10.5194/acp-11-6465-2011, 2011.

38) Ng, N. L., Canagaratna, M. R., Zhang, Q., Jimenez, J. L., Tian, J., Ulbrich, I. M., Kroll, J. H., Docherty, K. S., Chhabra, P. S., Bahreini, R., Murphy, S. M., Seinfeld, J. H., Hildebrandt, L., Donahue, N. M., DeCarlo, P. F., Lanz, V. A., Prevot, A. S. H., Dinar, E., Rudich, Y., and Worsnop, D. R.: Organic aerosol components observed in Northern Hemispheric datasets from Aerosol Mass Spectrometry, Atmos. Chem. Phys., 10, 4625–4641, doi: 10.5194/acp-10-4625-2010, 2010.

39) Ortega, A. M., Hayes, P. L., Peng, Z., Palm, B. B., Hu, W., Day, D. A., Li, R., Cubison, M. J., Brune, W. H., Graus, M., Warneke, C., Gilman, J. B., Kuster, W. C., de Gouw, J., Gutiérrez-Montes, C., and Jimenez, J. L.: Real-time measurements of secondary organic aerosol formation and aging from ambient air in an oxidation flow reactor in the Los Angeles area, Atmos. Chem. Phys., 16, 7411-7433, https://doi.org/10.5194/acp-16-7411-2016, 2016.

40) Ovadnevaite, J., O'Dowd, C., Dall'Osto, M., Ceburnis, D., Worsnop, D. R., and Berresheim, H.: Detecting high contributions of primary organic matter to marine aerosol: A case study, Geophys. Res. Lett., 38, L02807, doi: 10.1029/2010GL046083, 2011.

41) Ovadnevaite, J., Ceburnis, D., Leinert, S., Dall'Osto, M., Canagaratna, M., O'Doherty, S., Berresheim, H., and O'Dowd, C.: Submicron NE Atlantic marine aerosol chemical composition and abundance: Seasonal trends and air mass categorization, J. Geophys. Res. Atmos., 119, 11850–11863, doi: 10.1002/2013JD021330, 2014.

42) "Port Houston Statistics" Port Houston. http://porthouston.com/portweb/about-us/statistics/, Accessed August 9, 2017.

43) Ren, X., van Duin, D., Cazorla, M., Chen, S., Mao, J., Zhang, L., Brune, W. H., Flynn, J., Grossberg, N., Lefer, B. L., Rappengluck, B., Wong, K. W., Tsai, C., Stutz, J., Dibb, J. E., Jobson, B. T., Luke, W. T., and Kelley, P.: Atmospheric oxidation chemistry and ozone production: Results from SHARP 2009 in Houston, Texas, J. Geophys. Res. Atmos., 118, 5770-5780, doi: 10.1002/jgrd.50342, 2013.

44) Russell, L. M., Hawkins, L. N., Frossard, A. A., Quinn, P. K., and Bates, T. S.: Carbohydrate-like composition of submicron atmospheric particles and their production from ocean bubble bursting, P. Natl. Acad. Sci. USA, 107, 6652–6657, doi: 10.1073/pnas.0908905107, 2010.

45) Saarikoski, S., Carbone, S., Decesari, S., Giulianelli, L., Angelini, F., Canagaratna, M., Ng, N. L., Trimborn, A., Facchini, M. C., Fuzzi, S., Hillamo, R., and Worsnop, D.: Chemical characterization of springtime submicrometer aerosol in Po Valley, Italy, Atmos. Chem. Phys., 12, 8401–8421, doi: 10.5194/acp-12-8401-2012, 2012.

46) Sato, K., Takami, A., Kato, Y., Seta, T., Fujitani, Y., Hikida, T., Shimono, A., and Imamura, T.: AMS and LC/MS analyses of SOA from the photooxidation of benzene and 1,3,5-trimethylbenzene in the presence of NO_x: Effects of chemical structure on SOA aging, Atmos. Chem. Phys., 12, 4667-4682, https://doi.org/10.5194/acp-12-4667-2012, 2012.

47) Saunders, S. M., Jenkin, M. E., Derwent, R. G., and Pilling, M. J.: Protocol for the development of the Master Chemical Mechanism, MCM v3 (Part A): tropospheric degradation of non-aromatic volatile organic compounds, Atmos. Chem. Phys., 3, 161-180, https://doi.org/10.5194/acp-3-161-2003, 2003.

48) Schmale, J., Schneider, J., Nemitz, E., Tang, Y. S., Dragosits, U., Blackall, T. D., Trathan, P. N., Phillips, G. J., Sutton, M., and Braban, C. F.: Sub-Antarctic marine aerosol: Dominant contributions from biogenic sources, Atmos. Chem. Phys., 13, 8669–8694, doi: 10.5194/acp-13-8669-2013, 2013.

49) Schulze, B. C., Wallace, H. W., Flynn, J. H., Lefer, B. L., Erickson, M. H., Jobson, B. T., Dusanter, S., Griffith, S. M., Hansen, R. F., Stevens, P. S., VanReken, T., and Griffin, R. J.: Differences in BVOC oxidation and SOA formation above and below the forest canopy, Atmos. Chem. Phys., 17, 1805-1828, https://doi.org/10.5194/acp-17-1805-2017, 2017.

50) Setyan, A., Zhang, Q., Merkel, M., Knighton, W. B., Sun, Y., Song, C., Shilling, J. E., Onasch, T. B., Herndon, S. C., Worsnop, D. R., Fast, J. D., Zaveri, R. A., Berg, L. K., Wiedensohler, A., Flowers, B. A., Dubey, M. K., and Subramanian, R.: Characterization of submicron particles influenced by mixed biogenic and anthropogenic emissions using high-resolution aerosol mass spectrometry: Results from CARES, Atmos. Chem. Phys., 12, 8131-8156, doi: 10.5194/acp-12-8131-2012, 2012.

51) Sun, Y., Du, W., Fu, P., Wang, Q., Li, J., Ge, X., Zhang, Q., Zhu, C., Ren, L., Xu, W., Zhao, J., Han, T., Worsnop, D. R., and Wang, Z.: Primary and secondary aerosols in Beijing in winter: Sources, variations and processes, Atmos. Chem. Phys., 16, 8309–8329, doi: 10.5194/acp-16-8309-2016, 2016.

52) Tsimpidi, A. P., Karydis, V. A., Zavala, M., Lei, W., Molina, L., Ulbrich, I. M., Jimenez, J. L., and Pandis, S. N.: Evaluation of the volatility basis-set approach for the simulation of organic aerosol formation in the Mexico City metropolitan area, Atmos. Chem. Phys., 10, 525–546, doi: 10.5194/acp-10-525-2010, 2010.

53) Ulbrich, I. M., Canagaratna, M. R., Zhang, Q., Worsnop, D. R., and Jimenez, J. L.: Interpretation of organic components from Positive Matrix Factorization of aerosol mass spectrometric data, Atmos. Chem. Phys., 9, 2891–2918, doi: 10.5194/acp-9-2891-2009, 2009.

54) Vaughan, S., Ingham, T., Whalley, L. K., Stone, D., Evans, M. J., Read, K. A., Lee, J. D., Moller, S. J., Carpenter, L. J., Lewis, A. C., Fleming, Z. L., and Heard, D. E.: Seasonal observations of OH and HO_2 in the remote tropical marine boundary layer, Atmos. Chem. Phys., 12, 2149–2172, doi: 10.5194/acp-12-2149-2012, 2012.

55) Vong, R. J., Vong, I. J., Vickers, D., and Covert, D. S.: Size-dependent aerosol deposition velocities during BEARPEX'07, Atmos. Chem. Phys., 10, 5749-5758, doi: 10.5194/acp-10-5749-2010, 2010.

56) Wallace, H. W., Sanchez, N. P., Flynn, J. H., Erickson, M. H., Lefer, B. L., and Griffin, R. J.: Source apportionment of particulate matter and trace gases near a major refinery near the Houston Ship Channel, Atmos. Environ., 173, 16-29, doi: dx.doi.org/10.1016/j.atmosenv.2017.10.049, 2018.

57) Xu, J., Zhang, Q., Chen, M., Ge, X., Ren, J., and Qin, D.: Chemical composition, sources, and processes of urban aerosols during summertime in northwest China: insights from high-resolution aerosol mass spectrometry, Atmos. Chem. Phys., 14, 12593-12611, doi: 10.5194/acp-14-12593-2014, 2014.

58) Xu, J., Shi, J., Zhang, Q., Ge, X., Canonaco, F., Prévôt, A. S. H., Vonwiller, M., Szidat, S., Ge, J., Ma, J., An, Y., Kang, S., and Qin, D.: Wintertime organic and inorganic aerosols in Lanzhou, China: Sources, processes, and comparison with the results during summer, Atmos. Chem. Phys., 16, 14937–14957, doi: 10.5194/acp-16-14937-2016, 2016.

59) Zaveri, R. A., Voss, P. B., Berkowitz, C. M., Fortner, E., Zheng, J., Zhang, R. Y., Valente, R. J., Tanner, R. L., Holcomb, D., Hartley, T. P., and Baran, L.: Overnight atmospheric transport and chemical processing of photochemically aged Houston urban and petrochemical industrial plume, J. Geophys. Res., 115, doi: 10.1029/2009jd013495, 2010.

60) Zhang, Q., Jimenez, J. L., Canagaratna, M. R., Ulbrich, I. M., Ng, N. L., Worsnop, D. R., and Sun, Y.: Understanding atmospheric organic aerosols via factor analysis of aerosol mass spectrometry: a review, Anal. Bioanal. Chem., 401, 3045-3067, doi: 10.1007/s00216-011-5355-y, 2011.